J. Fluid Mech. (1977), *vol.* 79, *part* 3, *pp.* 553–594
Printed in Great Britain

Features of a separating turbulent boundary layer in the vicinity of separation

By ROGER L. SIMPSON, J. H. STRICKLAND† AND P. W. BARR

Department of Civil and Mechanical Engineering,
Southern Methodist University, Dallas, Texas 75275

(Received 31 December 1975 and in revised form 9 June 1976)

Measurements of a separating two-dimensional incompressible boundary layer with an airfoil-type pressure distribution are reported. Unique mean and fluctuation velocity measurements and the distribution of the fraction of the time γ_p during which the flow moves downstream were obtained in the separated region using a directionally sensitive laser anemometer. Linearized hot-film anemometer measurements of mean velocities, turbulent shearing stress and intensities, eddy speeds, spectra and dissipation were made for $\gamma_p > 0{\cdot}8$. The wall shearing stress, bursting frequencies, wall speed and spanwise structure were obtained using flush-surface hot-film sensors. The turbulent/non-turbulent interfacial intermittency γ and the frequency of passage of turbulent bulges were determined using smoke as a turbulence marker and the laser anemometer system for illumination and signal detection.

Upstream of separation the velocity profile correlations of Perry & Schofield (1973) are supported within the uncertainty of the data. Normal-stress effects are very important, influencing $-\overline{uv}/\overline{q^2}$ and the dissipation length correlations, and directly providing sizable terms in the momentum and turbulence energy equations. The criteria of Sandborn for turbulent separation and fully developed separation are found to hold. Downstream of separation there is apparent similarity of $\overline{u^2}$, U and γ_p throughout the shear flow. The passive low velocity backflow near the wall apparently just serves to satisfy continuity requirements after the energetic outer-region flow has deflected away from the wall upon separation.

The wall bursting frequency n_A scales on outer velocity and length scales, with $U_\infty/\delta n_A \approx 10$, or about twice the value observed for zero-pressure-gradient flows. The non-dimensional spanwise spacing of wall eddies is given approximately by the relation $\lambda_z U_M/\nu \approx 100$ upstream of separation, where $U_M = (-\overline{uv}_{\max})^{\frac{1}{2}}$. The speed of wall eddies is found to be about $14U_\tau$.

---

† Present address: Department of Mechanical Engineering, Texas Tech University, Lubbock, Texas.

1. Introduction

The experiments described in this paper are concerned with a nominally two-dimensional separating turbulent boundary layer produced by an adverse pressure gradient. An airfoil-type flow was used in which the flow was accelerated and then decelerated until separation. As pointed out by Samuel & Joubert (1974), very little experimental data are available for this case, which contains an increasingly adverse pressure gradient, even though there are many real flow situations such as ship hulls, aircraft wings and bodies of revolution where a portion of the streamwise pressure gradient distribution is increasingly adverse. In addition, few investigations, if any, have been concerned with the region with backflow downstream of the separation region (see Coles in Coles & Hirst 1969, pp. 1–45). It is thought (Sovran 1969) that this separated flow influences the free-stream potential flow, which in turn influences the upstream boundary-layer flow behaviour. Thus it is important that quantitative experimental results for a turbulent separated flow be obtained for better understanding of the flow's nature.

The use of well-established hot-wire techniques in separated flows is limited by the fact that such probes are generally not directionally sensitive. Consequently such hot-wire measurements are meaningless in regions where the flow changes direction. For this reason a directionally sensitive laser-Doppler anemometer was used to make the measurements in the smoke-seeded separated flow reported here. When possible hot-film measurements were also made for comparison. Earlier laser anemometer measurements in the downstream direction using a non-directionally sensitive system have been reported by Simpson, Strickland & Barr (1973). A new sampling signal processing method (Simpson & Barr 1975) was used for the measurements reported here, which alleviated some problems encountered in the earlier work.

The emphasis of this paper is on the significance of the experimental results and the features of this separating boundary layer that they reveal. These data provide a documented case against which turbulent shear-flow prediction methods can be tested. Many of the experimental details of the techniques for the measurements reported here are discussed at more length in previously published articles and these details are not reiterated here. The results for the flow examined here include the skin friction, mean velocity profiles, turbulent shearing stress and intensities, spectra, dissipation rate, turbulent/non-turbulent interfacial intermittency and frequency, downstream–upstream flow intermittency, and eddy speeds. Several methods of locating characteristics of the separation zone were used. Results for the wall bursting frequencies (Strickland & Simpson 1975) have already been reported, as have the techniques used to determine the spanwise variation of the instantaneous flow in the wall region (Simpson 1975).

2. Experimental equipment

The SMU wind tunnel with a test section 16 ft long and 3 ft wide was used to produce the desired boundary layer, which separated on the flat bottom wall as

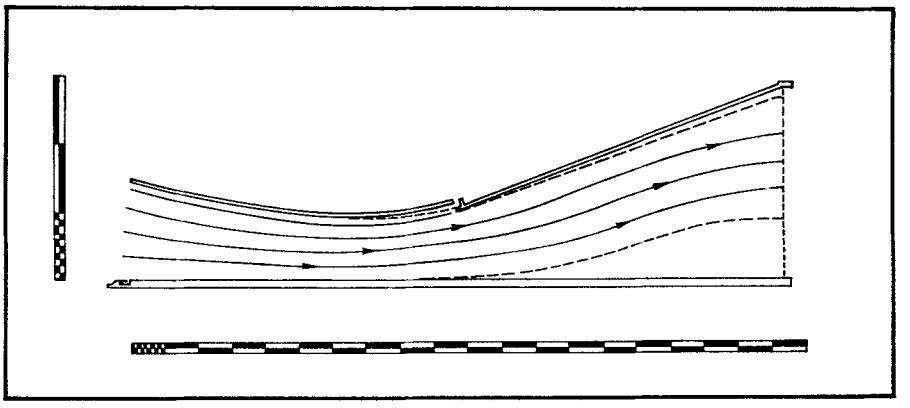

FIGURE 1. Schematic side view of the test section. Major divisions on scales are 10 in.; note 2:1 stretching of the vertical scale. Note baffle plate upstream of blunt leading edge on bottom test wall, upper-wall boundary-layer scoop and perforated metal exit plate. Equivalent inviscid streamlines are shown as solid lines with arrows; displacement-thickness distributions on top and bottom walls as broken lines.

shown in figure 1. Also shown in figure 1 are the mean streamlines of the equivalent inviscid free-stream flow and the measured top- and bottom-wall displacement-thickness distributions. The details of this tunnel as used in the current experiments are given by Strickland & Simpson (1973). This tunnel produces a free-stream flow uniform to within 0·05 % in the spanwise direction and to within 1 % in the vertical direction with a turbulence intensity level of 0·1 % at 60 ft s^{-1}. The adjustable top wall is Plexiglas while the side walls are constructed of float-plate glass to avoid dispersion of laser beams and laser anemometer signals.

The test-wall boundary layer is tripped by the blunt leading edge of the plywood floor, the height of the step from the wind-tunnel contraction up to the test wall being $\frac{1}{4}$ in. $1\frac{1}{4}$ in. upstream of the blunt leading edge, 33 smoke ports, $\frac{1}{8}$ in. in diameter, are located spanwise on $1\frac{1}{16}$ in. centres in the wind-tunnel contraction. A baffle plate deflects the smoke in the free-stream direction and tends to produce a uniform spanwise distribution of smoke. When smoke is not being used, air with a flow rate equal to the smoke flow rate is introduced through the smoke ports.

The smoke generator is of essentially the same design as that described by Echols & Young (1963), with the numerical values of particle size, flow rates and pressures being taken from their work. The smoke is produced by six nozzles each of which blows air at high speed through four orifices 0·04 in. in diameter into the liquid smoke material, which in this case is dioctal phthalate or 'DOP'. The DOP is atomized by the shearing action of the compressed air jets. A pressure drop of approximately 25 psi across the nozzle orifices is required to produce the desired effect. The total mass flow rate of the smoke system can be controlled by opening or closing valves to any of the six nozzles. The resulting mixture of air and DOP particles is blown perpendicular to the jets, towards the bottom of a 5 gallon impacter can, which removes any large particles which may have been

entrained in the mixture. The mixture is then blown out of the top of the impacter can into a manifold which distributes the smoke uniformly to the smoke ports in the wind-tunnel contraction.

In the experiments reported here, 3·3 $ft^3\ min^{-1}$ of smoke at a mass concentration of about $0{\cdot}3 \times 10^{-3}$ lb of smoke particles per cubic foot of blown air was used. The density of the undiluted smoke was only 0·4 % greater than that of air alone. In the test boundary layer near the separation region, the density of the diluted smoke was only about 0·0006 % greater than that of air alone, making smoke-induced density effects negligible. The mean particle size of this stable room-temperature (77 °F) smoke is approximately 1 μm. If a particle this size is accelerated from near rest to the free-stream velocity during a time δ/U_∞, as it may be when contained in some coherent structure, it will still follow the flow velocity to within 0·1 % according to the analysis of Brodkey, Hershey & Corino (1969). Mazumder, Hoyle & Kirsch (1974) report the frequency response of such a particle to be down 10 % at 10 kHz when subjected to sinusoidal oscillations. The spectral inertial subrange was below 10 kHz in the high velocity outer part of the boundary layer for this flow, so the particles were following the lower frequency oscillations found nearer the wall.

To eliminate preferential separation of the curved top-wall boundary layer, this layer was removed before the last 8 ft of the test section. The spanwise scoop removed about 5·5 % of the total tunnel mass flow. It was necessary to increase the static pressure at the scoop to produce this outflow. This was accomplished by placing a sheet of perforated metal over the test-section exit, which produced about a 0·06 in. of water excess over the ambient pressure at the scoop.

The laser anemometer system used a backscattering fringe-type arrangement and is discussed in detail by Simpson, Strickland & Barr (1974) and Simpson & Barr (1974, 1975). The argon-ion laser beam (4880Å) passed through an ultrasonic Bragg cell. The horizontal first-order diffracted beam, which was shifted 25 MHz, and the unshifted beam were focused to form real moving fringes in a volume 0·0125 in. in diameter and 1·140 in. long. Consequently the streamwise velocity component U could be measured as particles traversed the diameter of the probe volume. Signals greater than 25 MHz were obtained from fluid moving downstream while signals less than 25 MHz were obtained from fluid moving upstream. Signals received from this volume were focused onto the plane of a variable-aperture diaphragm and passed through a narrow-window (± 5 Å) interference filter to the face of a photomultiplier tube. All the optics were mounted on a single mobile cart which allowed movement along the wind-tunnel test section and provided for adjustment in all three directions. Laser power limitations prevented measurement of the normal velocity component V. With this optical arrangement it was not possible to measure W.

Sampling spectrum analysis of the signals was used because of the high signal drop-out level encountered in this flow with the low particle seeding level and the high signal frequencies produced by frequency shifting one incident beam. Most frequency trackers cannot handle either of these signal conditions. The basic principles of this signal processing method are explained here while more details are given by Simpson & Barr (1975). The signal from the photomultiplier tube

is input to a freely running swept filter spectrum analyser. For each sweep of the analyser when a particle happens to be in the focal volume, a vertical voltage distribution proportional to the filter output is displayed. The simultaneous horizontal sweeping voltage is linearly proportional to the signal frequency. The peak of the vertical voltage distribution marks the frequency of the signal due to the passing particle (Simpson & Barr 1975) and is used as a gating signal to allow the instantaneous value of the horizontal sweep voltage to be sampled. On the average about 30 data points per second were obtained with a spectrum-analyser sweep rate of 100 Hz. About 4000 data points were obtained for each velocity probability histogram.

Before gating the horizontal sweep voltage the vertical voltage distribution is fed into a pulse-shaping circuit which produces a pulse simultaneously with the occurrence of the peak value. This output pulse is used to trigger a sample-and-hold circuit into which the horizontal sweep voltage has been input. The sampled sweep voltage is held by the sample-and-hold circuit until a new signal from another particle is detected. The output of the sample-and-hold circuit is input to a SAICOR model 41 digital probability analyser to obtain a Gaussian-like histogram of output voltages which are related to particle velocities. From a histogram obtained for a given location in the flow, the mean streamwise velocity U, the mean-square streamwise fluctuation velocity $\overline{u^2}$, and the fraction of time γ_p that the flow moves downstream (downstream flow intermittency) were obtained from the relations

$$U = \sum_i \mathscr{U}_i \left(\frac{\Delta A}{A}\right)_i, \quad \overline{u^2} = \sum_i (\mathscr{U}_i - U)^2 \left(\frac{\Delta A}{A}\right)_i, \quad \gamma_p = \sum_{ip} \left(\frac{\Delta A}{A}\right)_{ip},$$

where $(\Delta A/A)_i$ is the fraction of the total histogram area for a given probability analyser bin corresponding to a velocity $\mathscr{U}$ and the subscript p denotes quantities corresponding to a positive velocity.

Standard Thermo-Systems, Inc., Model 1050 constant-temperature anemometers, Model 1055 linearizers, Model 1057 signal conditioners and a Model 1015C correlator were used in the experimental measurements reported here. Standard TSI Model 1274-10 normal-film, Model 1273-10 slant-film, and Model 1248-10 dual cross-film probes were used. For the speed measurements in the flow away from the wall, a two-sensor TSI Model 1244-10 probe was used with a 0·197 in. gap between the parallel sensors. The sensing elements for each of these probes are platinum-coated quartz rods 0·001 in. in diameter. Krohn-Hite Model 3202 (maximum flat) and 330B (RC) filters were used.

The hot-film sensors mounted flush with the surface were fabricated at SMU and are described in detail by Strickland & Simpson (1973). The basic sensing part is a very thin layer of platinum fired onto the end of a quartz rod of nominal diameter 2 mm. Gold leads were fired onto the sides of the rod and short wire leads were soldered to the gold. The resulting unit could be mounted in the wind-tunnel wall with the platinum portion flush with the test wall at various streamwise locations. A unit containing two flush-surface platinum sensors 0·020 in. in diameter was also fabricated to permit one of the sensors to be traversable. When the unit was located spanwise with zero spanwise spacing between the sensors,

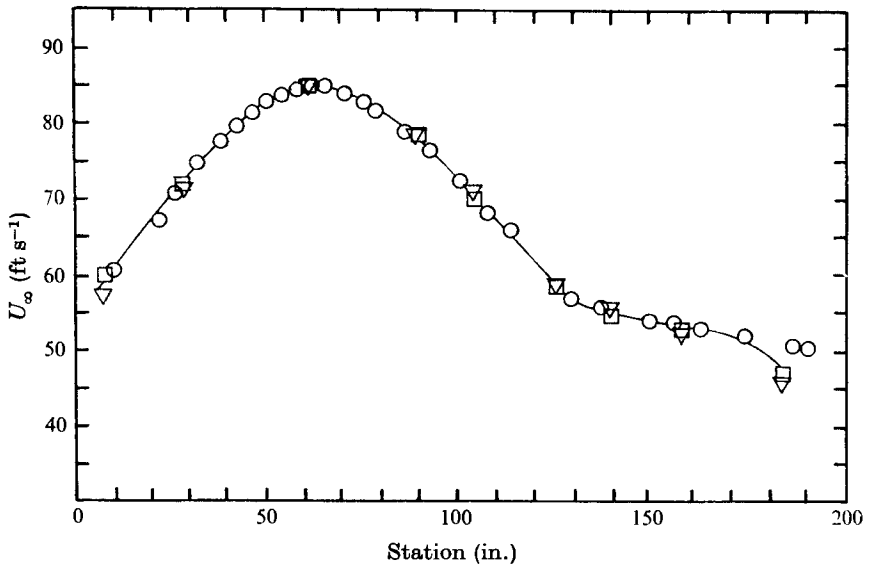

FIGURE 2. Free-stream velocity distribution. ○, from bottom-wall static taps; □ from bottom boundary-layer probe (Pitot); ▽, from top boundary-layer probe (Pitot).

the fixed sensor was located about 0·020 in. upstream of the movable sensor. No time delay in the maximum long-time cross-correlation between the sensor signals was detected, so these sensors were effectively at the same streamwise location. The constant-temperature frequency response for each sensor was determined to be down 3 dB at 4 kHz using the method of Freymuth (1967), the sensor widths were less than the mean spanwise variation of the instantaneous flow in the wall region, and the attenuation of spectra due to the finite element size was negligible for the low frequency range of interest.

3. Description of the test flow

Figure 2 shows the free-stream velocity distributions obtained along the tunnel centre-line using the stagnation pressure and the several noted static-pressure measurements. The agreement of these results indicates a rather uniform pressure across the free stream. Near the exit, the velocity calculated from the wall-tap data is seen to be about 5 % higher than that obtained using free-stream static pressures. This is due to the wall static pressure being lower than that in the free stream. This effect is primarily produced by the curvature of the free-stream flow towards the bottom wall as the perforated sheet-metal exit cover with its associated high pressure drop is approached.

Figure 3 shows the non-dimensional pressure gradient dC_p/dx measured along the centre-line of the bottom wall. Here $C_p \equiv (p-p_j)/\frac{1}{2}\rho U_{\infty j}^2$, where j denotes free-stream entrance conditions at $x = 0$. Just downstream of the location of the upper-wall scoop (96 in.), the slope of the static pressure gradient changes sign. Near 128 in. the pressure gradient abruptly drops to an approximately constant value downstream.

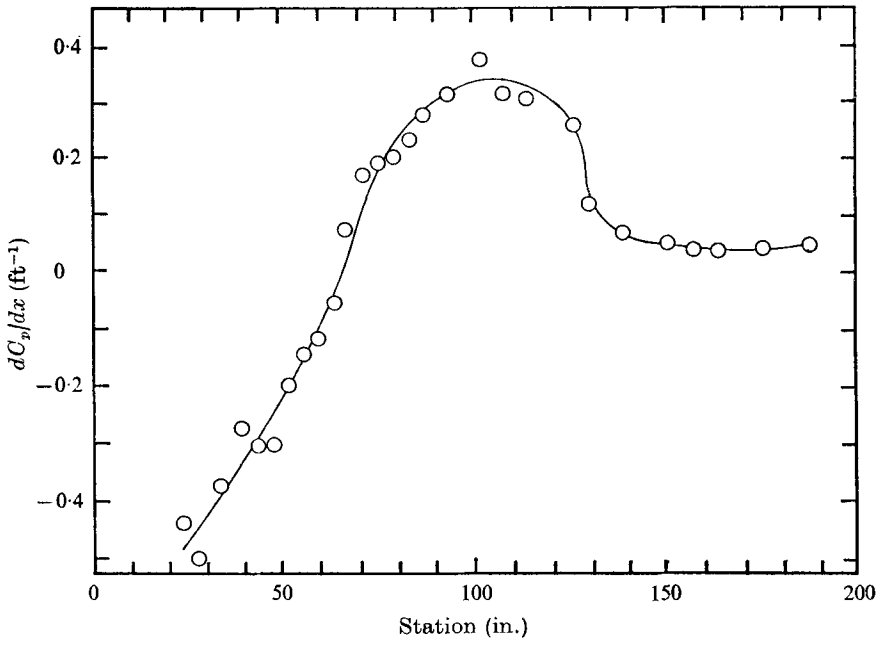

FIGURE 3. Pressure gradient along bottom wall.
$C_p = (p-p_j)/\frac{1}{2}\rho U_{\infty j}^2$; $U_{\infty j} = 53{\cdot}8$ ft s^{-1}.

In the bottom-wall boundary layer the static pressure at the wall is essentially equal to that at the boundary-layer edge except at the last station (183·6 in.). However, in the central portion of the boundary layer the static pressure tends to be less than that at the wall or free stream. Spangenberg, Rowland & Mease (1967) also noted such a phenomenon in their separating flow. This can first be discerned in the present flow at the station at 103·8 in., although the variation is only of the order of 0·003 in. of water with an uncertainty of about 0·002 in. of water. At the station at 157·1 in. the variation is approximately 0·020 in. of water. Rotta (1962) shows by use of the y-momentum equation that the static pressure in a boundary layer is less by an amount equal to $\overline{\rho v^2}$ than that in the free stream. This appears to account for the variation for stations up to 139·1 in. At the stations at 157·1 and 183·6 in. the factor $\overline{\rho v^2}$ accounts for only about $\frac{1}{3}$–$\frac{1}{2}$ of the variation. A significant pressure gradient normal to the wall is produced near 183·6 in. by exit-screen effects and is responsible for the lack of agreement at that station as discussed by Strickland & Simpson (1973).

Three-dimensionality of the mean flow is often thought to dominate separating boundary layers. Consequently, several types of measurement and observation were made to assess this condition. Boundary-layer velocity profiles using impact probes were obtained to examine the upper-wall and bottom-wall flow behaviour (Strickland & Simpson 1973). Mean streamwise velocity profiles taken across the central 12 in. of the bottom wall indicate that the flow was two-dimensional to within about 1 ft s^{-1}. Wall static pressures measured in the same region are within 1 % of the dynamic pressure of being uniform across the flow. Consideration

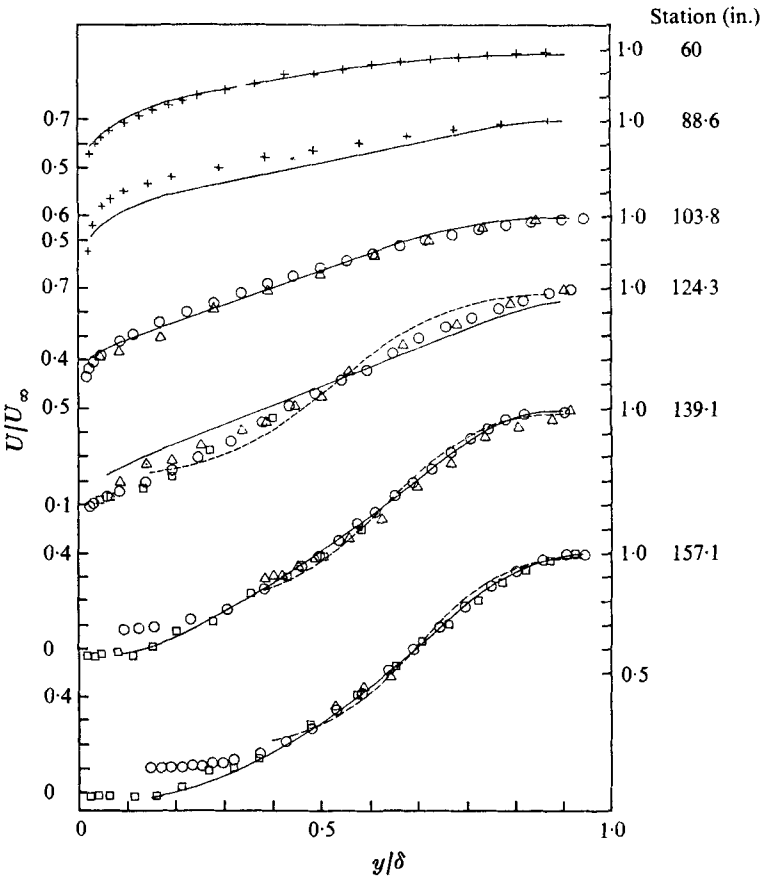

FIGURE 4. Mean velocity profiles: +, impact probe; ○, normal hot film; △, laser anemometer, Simpson *et al.* (1973); □, present laser anemometer. Solid lines: stations at 60 and 88·6 in., prediction of Bradshaw *et al.* method; stations at 103·8 and 124·3 in., correlation of Perry & Schofield; stations at 139·1 and 157·1 in., visual aid only. – – –, equation (13).

of mass-flow balance indicates that the effective convergence of the flow owing to growth of the side-wall boundary layers introduces some small three-dimensionality. The maximum convergence occurs near the station at 120 in. and is approximately 0·07 in. per in. of flow length. Prediction of this flow up to separation by the method of Bradshaw, Ferriss & Atwell (1967), with and without the measured convergence, indicates that convergence had a negligible effect. Collins & Simpson (1976) found that the two-dimensional momentum integral equation in the form used by Coles & Hirst (1969) was satisfied near separation to within 3% of the surface shear-stress term when normal-stress terms were properly included.

Data obtained with the Model 1273–10 probe (sensor slanted at 45° to the stem) were also used to obtain an estimate of the cross-flow velocity along the tunnel centre-line. By obtaining mean voltage signals at different stem orientations, the W and U components could be deduced at a given spatial location. Results obtained upstream of the station at 124·8 in. indicate negligible cross-

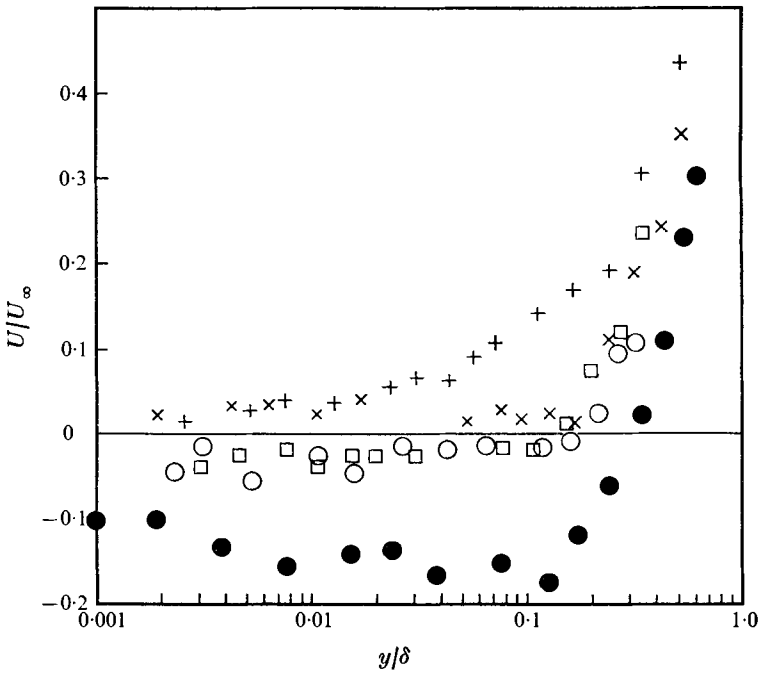

FIGURE 5. Mean velocity profiles near the wall in the separation region: +, 124·6 in.; ×, 132·2 in.; □, 139·1 in.; ○ 156·0 in.; ●, 165·8 in.

flow within the small uncertainty of aligning the probe with the tunnel centre-line. Downstream the peak values of W appear in regions near the wall where the mean velocity U is small. The value of W in these regions is less than 1·5 ft s^{-1} or about 3 % of the free-stream velocity. However, as discussed below, intermittent flow separation and backflow occur in these regions so these results from the directionally insensitive hot-film sensor are suspect.

Some small light solid particles were introduced at the downstream portion of the separation zone, moved randomly from side to side and back and forth for a short time, then migrated upstream until a dune, straight to within about 2 in., was formed perpendicular to the streamwise direction across the tunnel floor. This indicates that in a mean-flow sense the aerodynamic forces acting on these particles were evenly balanced across the flow in this zone in the vicinity of separation. Thus, within the uncertainty of the instrumentation and techniques employed, the apparent mean three-dimensionality uncovered by all of these measurements appears to be minimal upstream of the station at 124·8 in. and small downstream.

4. Experimental results for the mean flow

Figures 4 and 5 present laser anemometer results for the mean velocity along with downstream flow results from the normal hot-film and impact probes. Table 1 presents characteristic parameters for this flow. The laser anemometer results were obtained from two different optical systems at different times, with

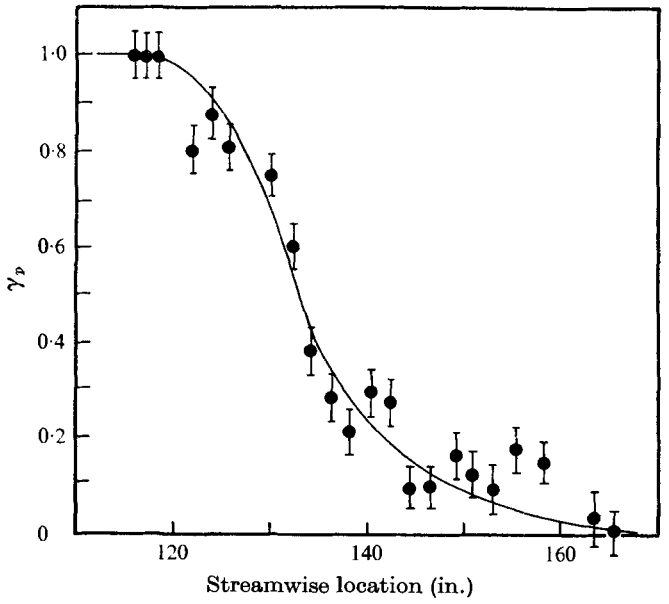

FIGURE 6. Fraction of time that the flow 0·010 in. from the wall is in the downstream direction. Solid line for visual aid only.

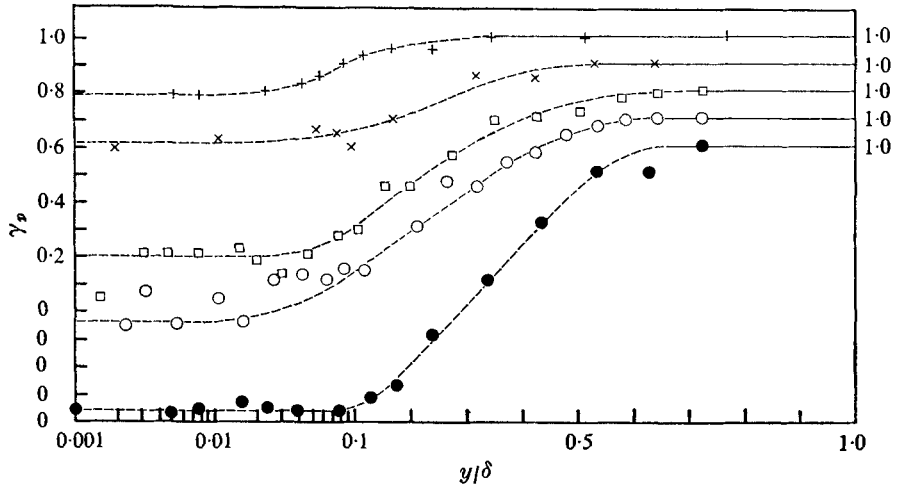

FIGURE 7. Fraction of time γ_p that the flow is in the downstream direction. Note abscissa scale change and displaced ordinate. Symbols same as in figure 5. Lines for visual aid only.

the earlier apparatus not containing a Bragg cell and therefore incapable of measuring backflows. Turbulence intensity measurements from the earlier work (Simpson *et al.* 1973) were known to be in error owing to dispersion bandwidth limitations of the spectrum analyser used at that time. The signal processing technique described above and by Simpson & Barr (1975) alleviated that problem. However, good agreement between these two sets of mean velocity results is observed for $\gamma_p \approx 1$, where γ_p is the fraction of time that the flow is downstream.

Station (in.)	Re_θ	U_∞ (ft s^{-1})	dU_∞/dx (s^{-1})	$\frac{1}{2}C_f \times 10^3$§	$\delta_{0.99}$ (in.)	$H = \delta^*/\theta$
28·2	2240	71·6	8·1	2·06†	0·69	1·29
60·0	3520	85·0	0·60	1·73	0·82	1·33
88·6	6020	78·0	−5·2	1·30	1·25	1·39
103·8	9220	70·8	−6·15	0·83†	1·82	1·63
108·8	10100	67·6	−6·6	0·74	2·13‡	—
117·8	13600	62·8	−6·9	0·20	2·89‡	—
124·3	17700	58·9	−5·9	0·113	3·71	2·62
126·8	18400	57·6	−4·6	0·08	3·90‡	—
136·0	21100	56·0	−2·0	−0·06	5·34‡	—
139·1	21400	55·5	−1·75	−0·06	6·54	4·63
148·0	22600	54·2	−1·5	−0·3	7·3‡	—
157·1	24000	53·3	−1·0	−0·1	9·38	5·36
165·8	25700	52·7	−1·0	−0·14	10·2‡	—
175·7	30000	51·6	−1·1	−0·14	11·4‡	—
184·5	38000	50·7	−1·2	−0·15	12·23	—

† Solid line, figure 12.
‡ Interpolated value.
§ Interpolated value from results from surface hot film (Simpson *et al.* 1973).

TABLE 1. Values of parameters along the flow. $\nu = 1{\cdot}68 \times 10^{-4}$ ft^2 s^{-1}.

Simpson *et al.* (1973) have noted good agreement between impact-probe and hot-film mean velocity profiles for the flow in the downstream direction, accounting for turbulence intensity effects.

Figure 6 shows values of γ_p measured 0·010 in. from the test wall while figure 7 shows γ_p profiles at the various streamwise stations. Simpson (1976) pointed out that, with the Gaussian velocity probability distribution that is obtained near separation, intermittent backflow occurs when the local turbulence intensity $(\overline{u^2})^{\frac{1}{2}}/U$ exceeds $\frac{1}{3}$, where U is the local mean velocity. Intermittent backflow near the wall is observed as far upstream as 120 in. Unfortunately, because the laser anemometer signal is not continuous, the frequency of flow reversal could not be determined. For $\gamma_p > 0{\cdot}8$, we can see from figure 4 that the normal hot-film data agree with the laser anemometer results, even though some effect of signal rectification is present for the hot film.

Also since the laser anemometer signal was not continuous, it was not possible to conditionally sample more than one quantity at a time with available equipment. Thus only U was conditionally analysed, to obtain the average positive velocity U_p and the average negative velocity U_n. These quantities are related to U and γ_p through

$$U \equiv U_p \gamma_p + (1-\gamma_p) U_n.$$

Like U and γ_p near the wall in the separation zone, U_p and U_n have rather flat profiles (Simpson *et al.* 1974), indicating no dominant mean positive or mean negative velocity structure.

Laser anemometer signal effects on the mean-square fluctuation $\overline{u^2}$ were found to be negligible for the data presented here (Simpson *et al.* 1974; Simpson 1976). The effects examined were transit-time broadening, velocity-gradient broaden-

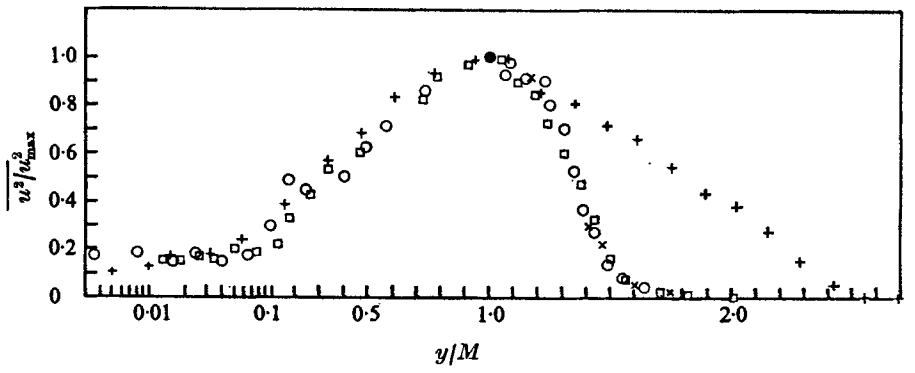

FIGURE 8. Streamwise normal stress in the separated region normalized by the maximum stress and the distance from the wall to the maximum.

	Location (in).	M/δ	$(\overline{u^2}/U_\infty^2)_{max}$	$(U/U_\infty)_{M/\delta}$
+	124·6	0·40	$17{\cdot}6 \times 10^{-3}$	0·47
⊡	139·6	0·58	27×10^{-3}	0·52
⊙	157·1	0·65	36×10^{-3}	0·52
×	183·6	0·66	58×10^{-3}	0·59

ing, and high velocity particle biasing. Good agreement of these data was obtained with $\overline{u^2}$ from the cross-film probe for $\gamma_p > 0{\cdot}95$. Velocity probability diagrams obtained using the normal hot film indicated a double-peak rectified distribution for $\gamma_p < 0{\cdot}95$ owing to directional insensitivity of the sensor, and thus much lower values of $\overline{u^2}$ than the laser results as shown in figure 9 (*a*). Simpson (1976) discussed the rectification effect on hot films or hot wires in more detail.

Figure 8 shows $\overline{u^2}/(\overline{u^2})_{max}$ *vs.* y/M for the downstream separated flow stations, where $\overline{u^2}_{max}$ and M are the maximum mean fluctuation and its location for that profile. The observed similarity is fairly good for $y/M < 1$ even at the station at 124·6 in., where $\gamma_p \geqslant 0{\cdot}8$. At all other stations shown in that figure, similarity holds throughout the profiles. It is interesting to note that γ_p appears to approach unity for each profile in the vicinity of the maximum $\overline{u^2}$ value observed. A plot of $\overline{u^2}/U^2$ *vs.* x for points 0·010 in. off the wall shows that the maximum value occurs near 132 in., which is consistent with the location of $\gamma_p = 0{\cdot}5$ shown in figure 6, the location of zero mean wall shearing stress shown in figure 12, and the maximum surface hot-film fluctuation signals presented by Simpson *et al.* (1973).

The hot-film data for U, $\overline{uv}$, $\overline{u^2}$, $\overline{v^2}$ and $\overline{w^2}$ from the cross-film probe were corrected for longitudinal cooling using Champagne & Sleicher's (1967) correction. This correction was verified before these measurements were made. At several stations data were obtained using the slanted hot film in several orientations, the data reduction equations accounting for the response to flow over and along the sensor. Figure 9 shows the various $\overline{u^2}$, $\overline{v^2}$ and $\overline{w^2}$ profiles obtained, along with $\overline{u^2}$ from the laser anemometer. Data for $\overline{v^2}$ and $\overline{w^2}$ are not presented for $\gamma_p < 0{\cdot}8$ since they would be meaningless. The scatter among the $\overline{u^2}$ results for $\gamma_p = 1$ obtained by different methods still indicates agreement well within 10 % for most of the data.

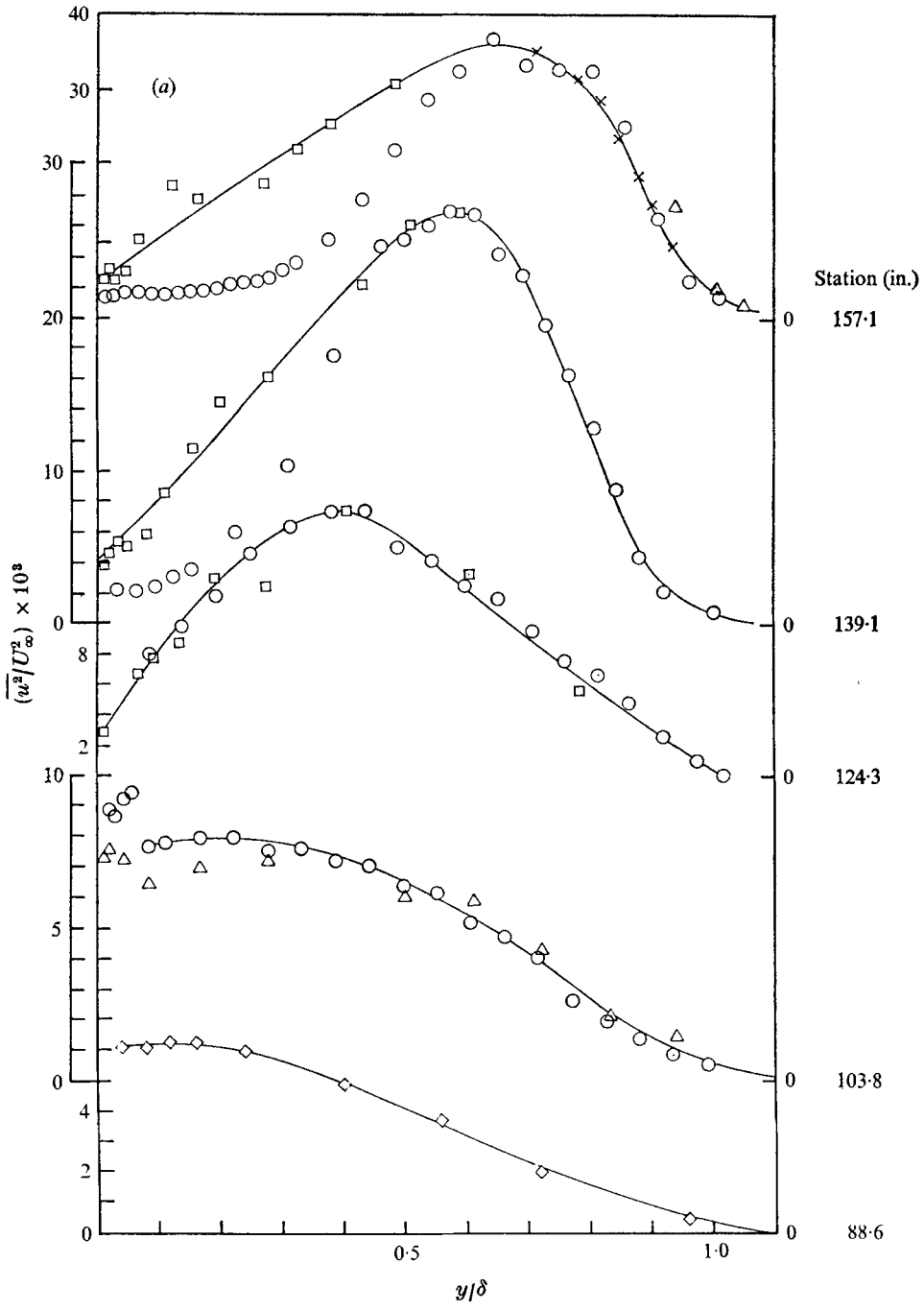

FIGURE 9 (*a*). For legend see p. 567.

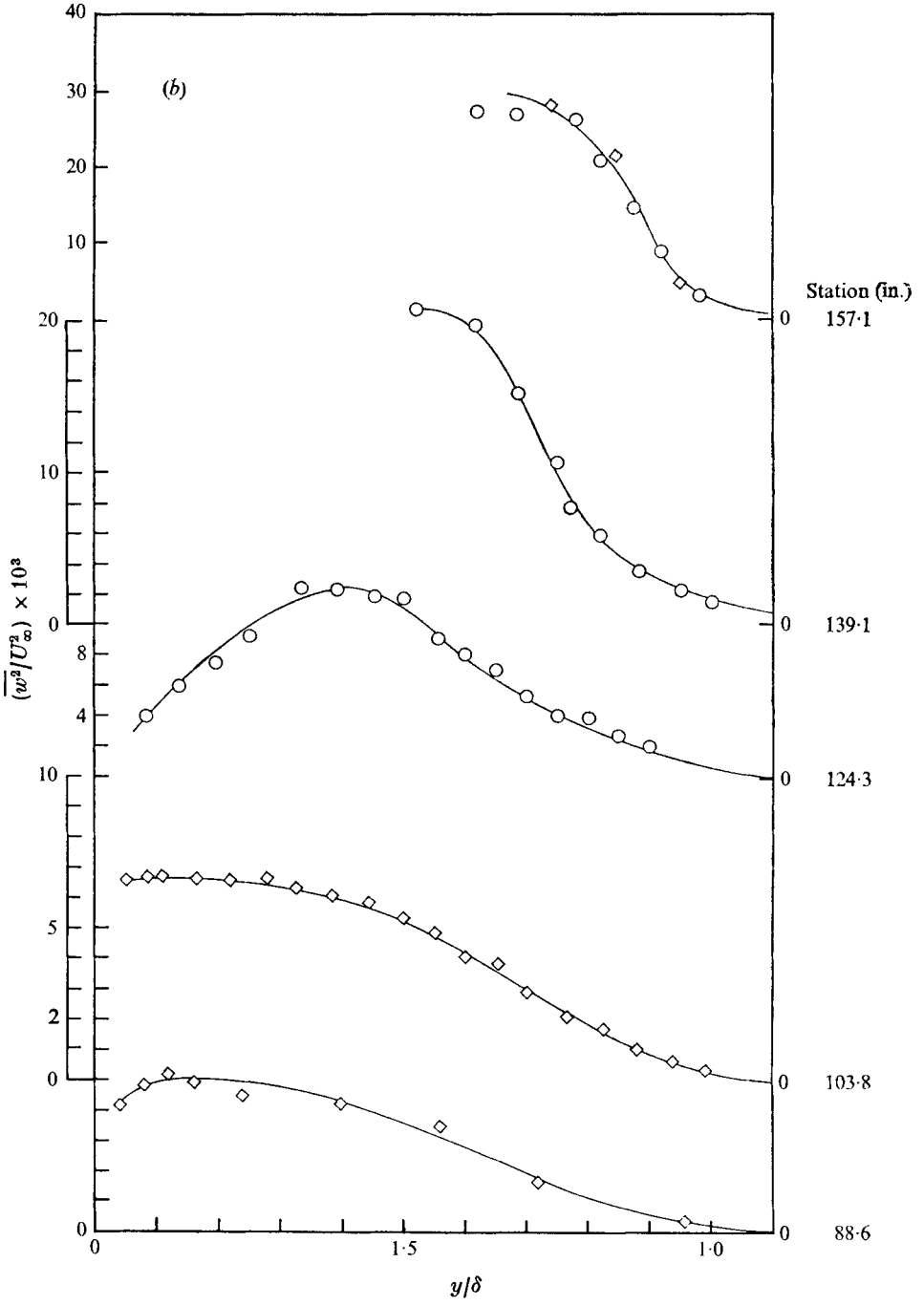

FIGURE 9(*b*). For legend see p. 567.

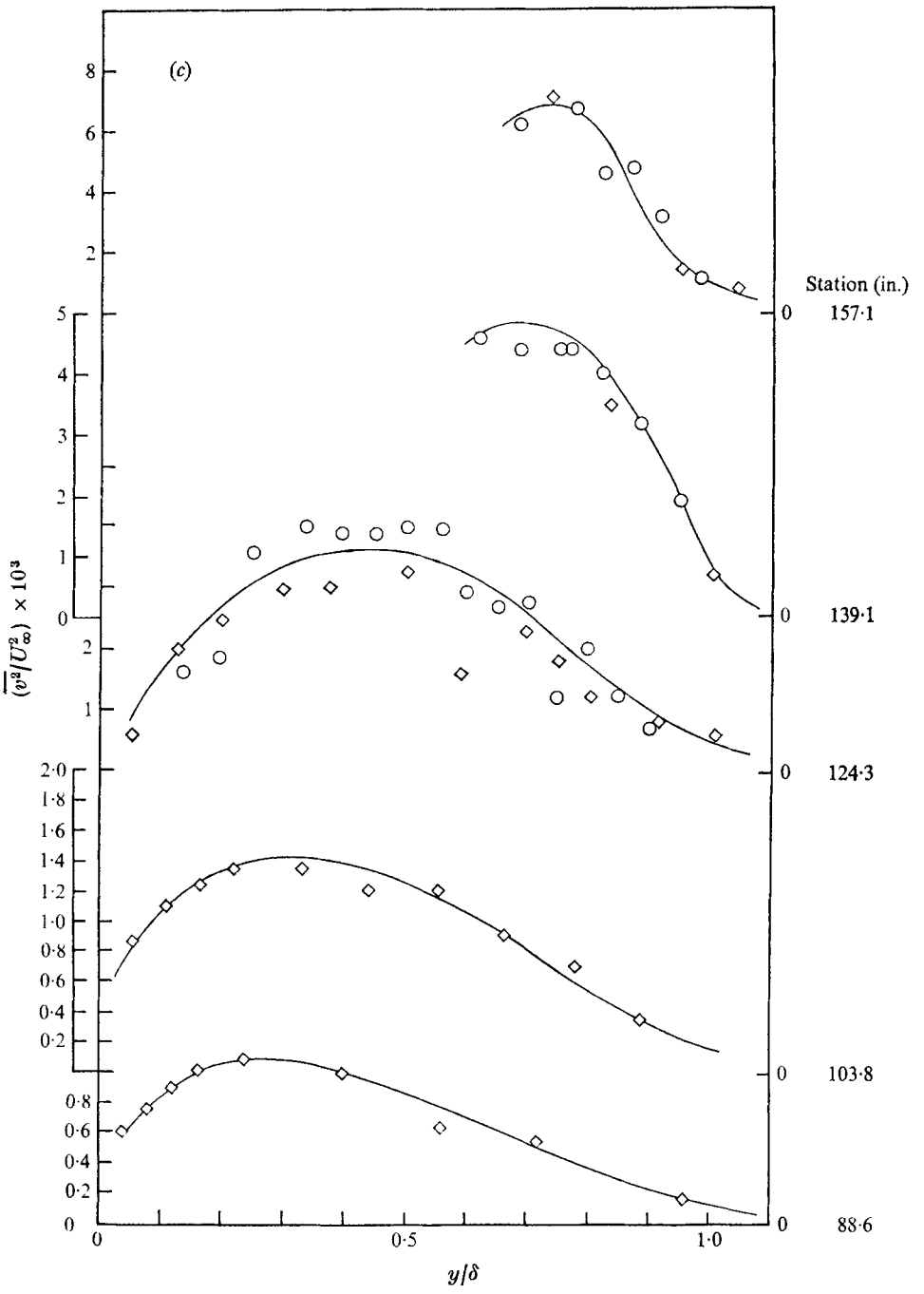

FIGURE 9. (*a*) $\overline{u^2}/U_\infty^2$ distributions: ○, normal hot film; △, laser anemometer, Simpson *et al.* (1973); □, present laser anemometer; ×, cross-film; ◇, slanted hot film. (*b*) $\overline{w^2}/U_\infty^2$ and (*c*) $\overline{v^2}/U_\infty^2$ distributions: ○, cross-film; ◇, slanted hot film. Solid lines for visual aid only. Note displaced ordinates.

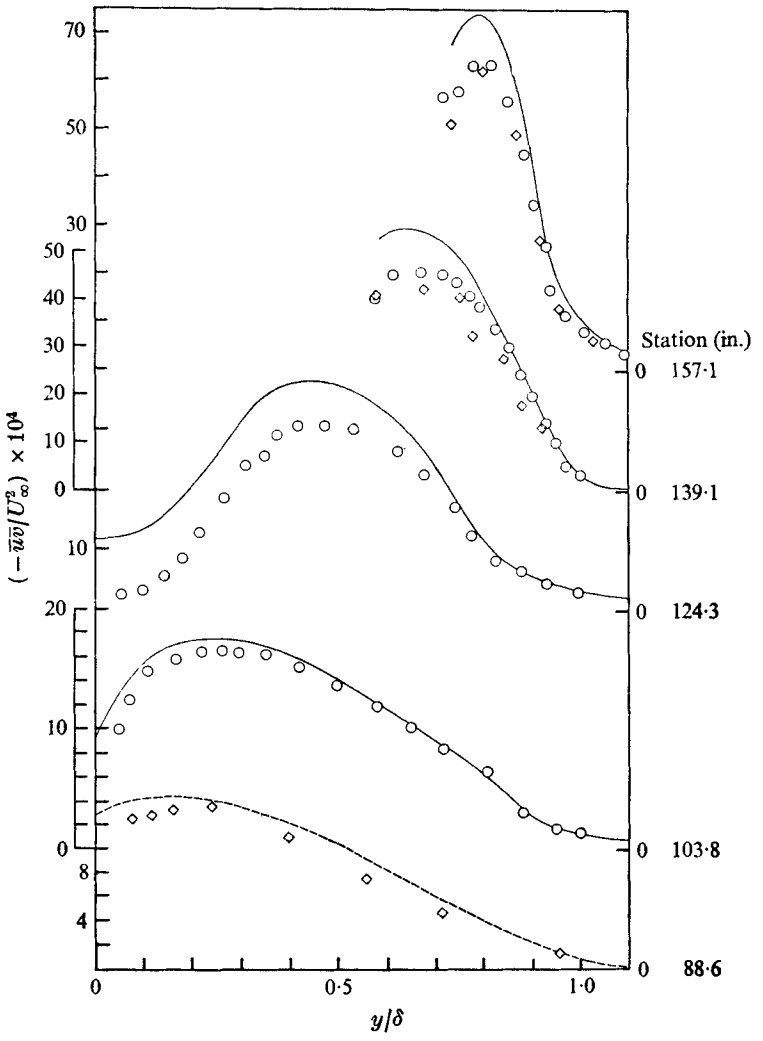

FIGURE 10. $-\overline{uv}/U_\infty^2$ distributions: ○ cross-film; ◇ slanted hot film. —, pseudo-shearing-stress distributions; – – –, prediction of Bradshaw *et al.* (1974) method. Note displaced ordinates.

The results for $\overline{v^2}$ and $\overline{w^2}$ are approximately 30 % and 45 % uncertain, respectively, as estimated by the single-sample uncertainty method of Kline & McClintock (1953), but agreement between the results obtained by each probe is somewhat better than that.

Figure 10 presents $-\overline{uv}/U_\infty^2$ for the various stations for $\gamma_p > 0{\cdot}95$. The $\overline{u^2}$ results from the slanted hot-film or the cross-film probe were within 5 % of the normal hot-film results when $-\overline{uv}$ measurements were made. So & Mellor (1973) indicated that $-\overline{uv}$ values from their slanted hot wire were apparently low when the sensor was less than about two wire lengths from the wall. Consequently, no $-\overline{uv}$ measurements were attempted here closer than about 0·1 in. from the wall with either the slanted or the cross-film probe. Agreement between measure-

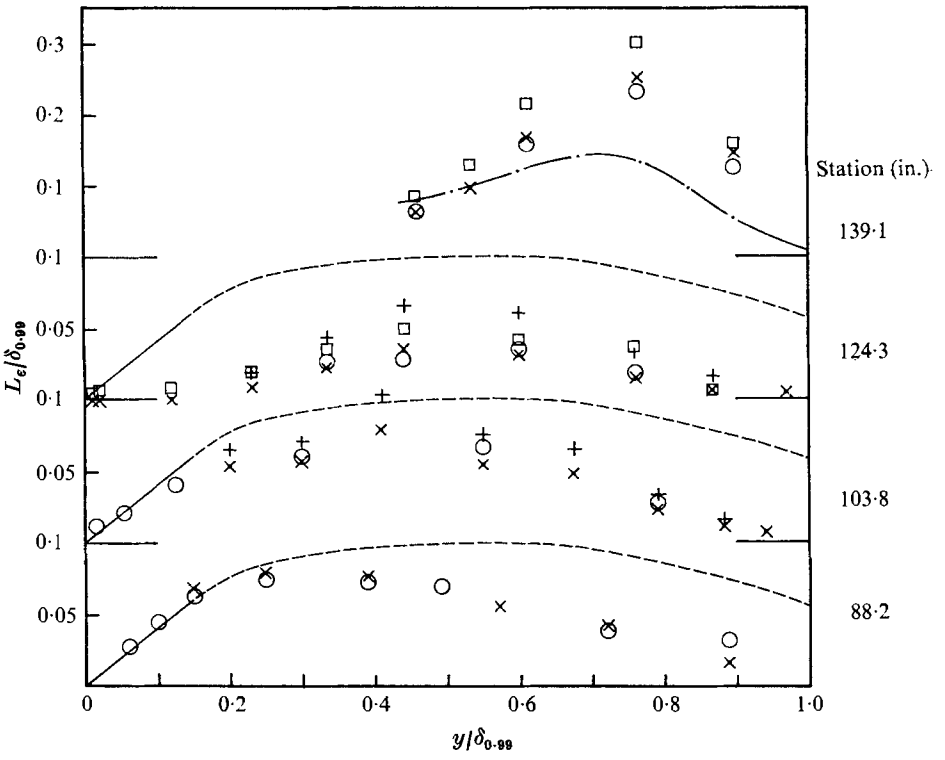

FIGURE 11. Dissipation-length distributions at the various stations: ○ spectra result; ×, differentiator result and measured $-\overline{uv}$; □, differentiator result and pseudo-shearing stress; +, differentiator result and $-\overline{uv}F$. ——, $L_\epsilon/\delta_{0\cdot99} = 0\cdot4(y/\delta_{0\cdot99})$; – – –, distribution of Bradshaw (1967*a*); —·—, Wygnanski & Fiedler (1970).

ments made at the same station by the two probes is within 20 % while the uncertainty of each measurement was estimated to be about 11 %.

Spectral data for $\overline{u^2}$ were obtained for $\gamma_p = 1$ using the normal hot-film probe; they were then used together with the $-\frac{5}{3}$ law of the inertial subrange in the manner of Bradshaw (1967*a*, *b*) to estimate the turbulence energy dissipation rate. The dissipation rate was also estimated using the assumption of local isotropy and Taylor's hypothesis for convection velocities, i.e. $\epsilon = 15\nu\overline{(\partial u/\partial t)^2}U^{-2}$. Results of determining $\overline{(\partial u/\partial t)^2}$ from signal differentiation and from

$$\overline{u^2}\int_0^\infty n^2F(n)\,dn$$

were in all cases within 5 %. The correction for finite wire length of Wyngaard (1969) was applied.

Figure 11 shows the dissipation results in terms of the dissipation length L_ϵ used by Bradshaw *et al.* (1967):

$$\frac{L_\epsilon}{\delta} = \frac{(\tau/\rho)^{\frac{3}{2}}}{\epsilon\delta}.$$

Agreement between the spectra and differentiator results is within 20 % at the stations at 88·2 and 103·8 in. but is somewhat poorer at the downstream stations. Also shown is the dissipation-length distribution $L_\epsilon/\delta = 0{\cdot}4y/\delta$ near the wall. Well upstream of separation, agreement of the measurements with this relation is good, but downstream the dissipation near the wall decreases more slowly than does the shear stress. The results when $\gamma_p < 1$ at the station at 124·3 in. should be viewed cautiously. The dissipation-length distribution of Bradshaw (1967*a*) is also shown, here in terms of $\delta_{0{\cdot}99}$ instead of his $\delta_{0{\cdot}995}$ ($\delta_{0{\cdot}995} \approx 1{\cdot}05\delta_{0{\cdot}99}$). Nowhere is agreement good except near the wall upstream of separation. These results are discussed further in §6.

With the results for the station at 139·1 in. are shown the dissipation-length results deduced from the measurements of Wygnanski & Fiedler (1970) for the high velocity edge of a mixing layer. For this plot the mixing-layer results were length scaled such that the shapes of the shear-stress distributions outwards from the maxima matched. The reason for the humps in both L_ϵ/δ profiles is that the dissipation maxima occur closer to the low velocity regions than the shear-stress maxima. Both profiles have roughly the same shape, which suggests that the outer separated flow behaves somewhat like the high velocity edge of a mixing layer. Upstream of separation the microscale λ was about 0·07 in. in the centre of the boundary layer while downstream it was about 0·2 in. This indicates that before separation dissipation is much more intense compared with the available turbulence energy than downstream.

Four different ways of deducing the mean wall shearing-stress distribution were used: the velocity profile cross-plot method used by Coles & Hirst (1969), the Preston-tube technique, hot-film sensors mounted flush with the surface and the Ludwieg & Tillmann skin-friction correlation. The results were reported by Simpson *et al.* (1973). The hot-film sensors mounted flush with the surface were also used to deduce shearing-stress fluctuations. The cross-plot, Preston-tube and Ludwieg & Tillmann methods require the existence of a universal logarithmic law of the wall. All velocity profiles obtained upstream of and at the station at 124·3 in. indicated similar logarithmic regions described by equation (8) below.

The agreement of the values of the mean wall shearing stress obtained by the various methods is reasonably good. Estimated uncertainties for each type of result were computed, the largest uncertainties occurring at the station at 124·3 in. The Coles cross-plot and the Ludwieg–Tillmann methods, which use hot-film velocity profile data, the flush hot-film and the Preston tube produce results within $\pm$ 16 % at this station. Considering the small value of $\frac{1}{2}C_f$ being measured, this agreement is gratifying. These results are shown in figure 12. The data obtained using the flush-mounted hot-film sensors are not dependent on the notion of a logarithmic wall region. This would tend to suggest that the law of the wall is valid until near the location where γ_p is first less than one at the wall, since there appears to be reasonable agreement between flush-mounted hot-film data and the methods which use the law of the wall.

The fact that only absolute shearing stresses are detected explains in part why a mean shearing stress equal to zero was never observed from the flush-mounted hot-film data in the region of separation. Since time-averaged backflow was

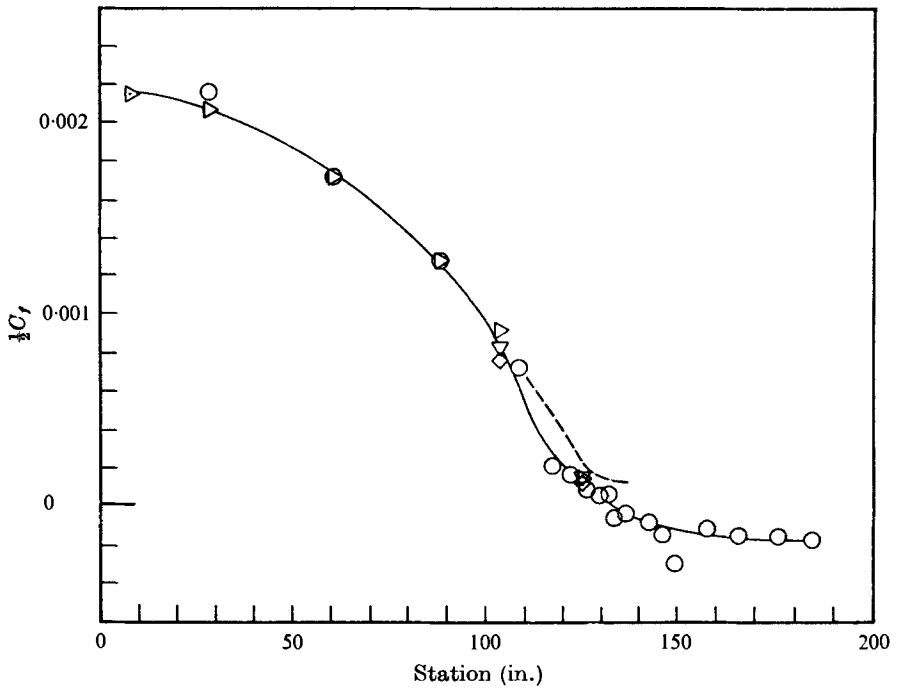

FIGURE 12. Friction-factor distributions: ○, flush hot film; ▷, Preston tube; ◇, cross-plot of hot-film data; ▽, from Ludwieg & Tillmann relation (Simpson *et al.* 1973). ——, for visual aid only; – – –, prediction of Bradshaw *et al.* (1974) method.

observed downstream of 132 in. by laser anemometer measurements near the wall, those shearing stresses are presented as negative values. No attempts to correct the mean shearing stresses in the separation region for the rectification effect have been made for the results shown in figure 12.

5. Experimental results on the flow structure

Bursting and spanwise structure of sublayer

In the past fifteen years it has come to be recognized that the eddy structure in the viscous sublayer of a turbulent boundary layer or duct has preferred eddy shapes and spacings, easily observed by flow-visualization techniques and leading to periodicity in correlation measurements. It appears from the work of other experimentalists (Gupta, Laufer & Kaplan 1971; Kline *et al.* 1967; Bakewell & Lumley 1967; Corino & Brodkey 1969; etc.) that there is a periodic lift-off or bursting sequence in the sublayer in which a hairpin or horseshoe vortex-like structure is formed (Willmarth 1975). Kim, Kline & Reynolds (1971) obtained frequencies from autocorrelations of this quasi-periodic behaviour over short times of about 30 burst periods for which the phenomena remained coherent. The counter-rotating trailing legs of these apparent vortices, as they are formed side by side, produce fluctuations in the sublayer that are periodic in the spanwise or Z direction on a short time scale. The data of Gupta *et al.* indicate that the

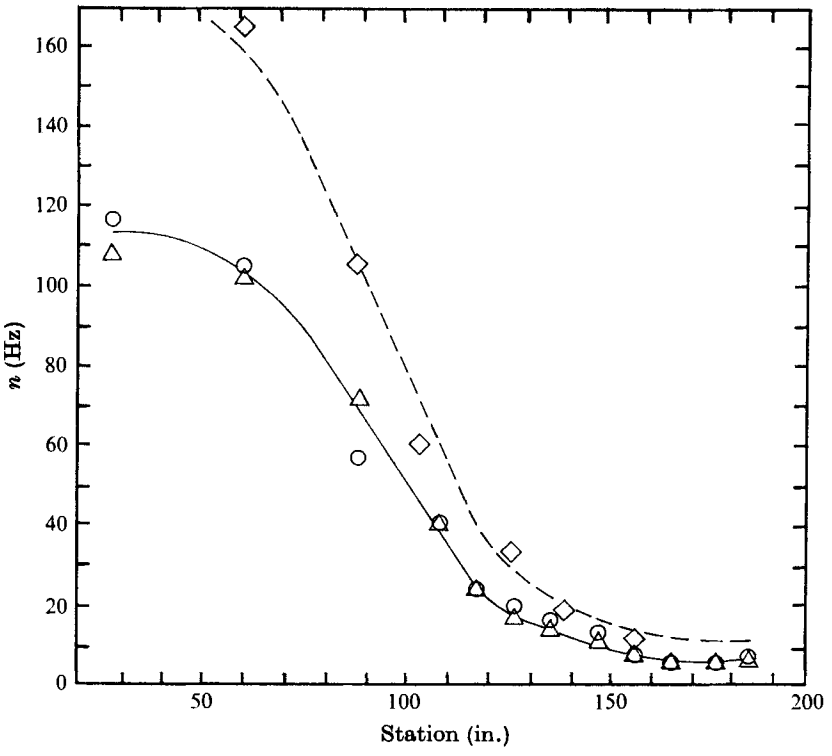

FIGURE 13. Bursting and intermittency frequencies. ○, autocorrelation; △, spectra bursting results; ◇, intermittency results. Lines for visual aid only.

'short-time' normalized cross-correlation of fluctuations $s\hat{R}_{uu}(Z, T_s)$ can be represented by a spanwise-periodic function. In this case $s\hat{R}_{uu}(Z, T_s)$ was defined as $sR_{uu}(Z, T_s)/sR_{uu}(0, T_s)$, where

$$sR_{uu}(Z, T_s) = \frac{1}{T_s}\int_t^{t+T_s} u(0,t)\,u(Z,t)\,dt - \left(\frac{1}{T_s}\int_t^{t+T_s} u(0,t)\,dt\right)\left(\frac{1}{T_s}\int_t^{t+T_s} u(Z,t)\,dt\right).$$

Their results indicate that the sampling time T_s over which the cross-correlation is averaged must be less than about 20 bursting periods in order for the periodic spanwise structure to be detectable. These quantities have not previously been measured in a boundary layer with a strong adverse pressure gradient.

Strickland & Simpson (1973, 1975) assumed that the short autocorrelation time scale from a flush-mounted hot-film sensor was equal to the bursting period. Histograms of the frequency characterized by the time to the first peak in these autocorrelations were constructed and the frequency corresponding to the peak in each histogram was taken as the characteristic frequency. The histograms appeared to have a lognormal probability distribution, so this peak frequency was also the median frequency. Strickland & Simpson also noted a one-to-one correspondence between this characteristic frequency and the peak in the first moment of the spectra $nF(n)$ of wall shearing stress. Also, examination of spectral data from zero-pressure-gradient boundary layers produced bursting frequencies

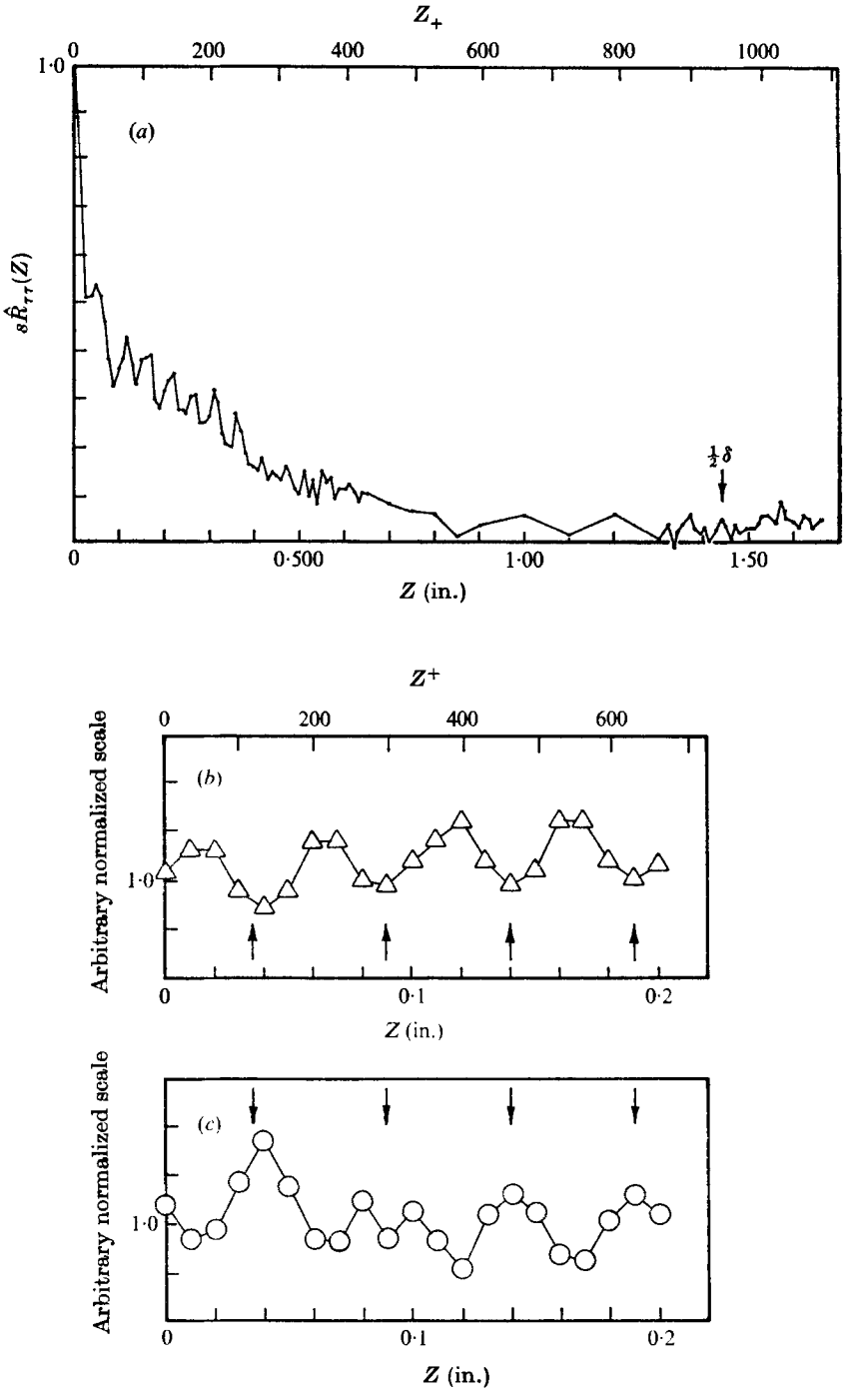

FIGURE 14. Station at 117·8 in. (*a*) Long-time spanwise correlation results. Amplitude probability distribution results: (*b*) the largest positive pulse recorded *vs.* Z; (*c*) the maximum probability value *vs.* Z; arrows denote local minima shown in (*a*). Experimental data points are connected by solid lines for visual aid only.

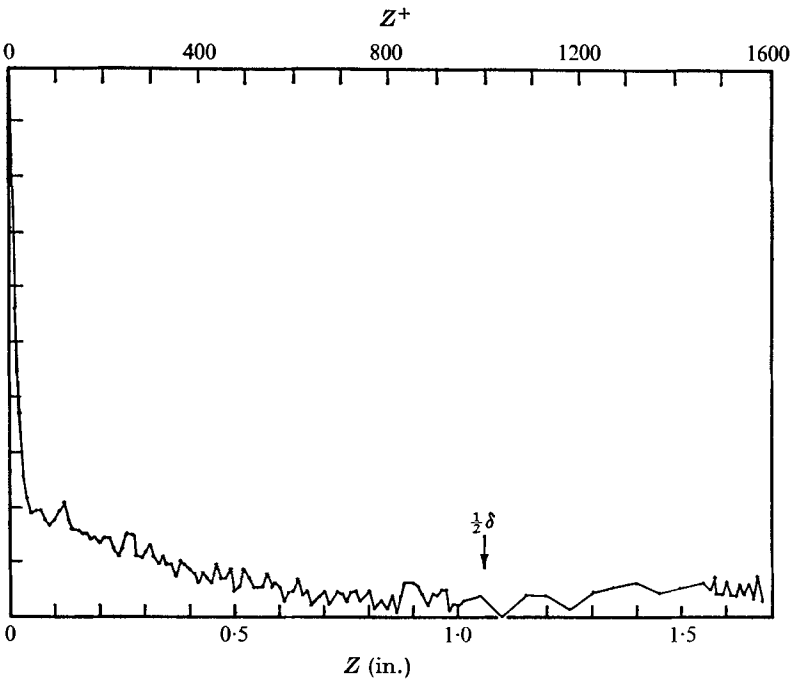

FIGURE 15(*a*). For legend see facing page.

in agreement with those previously reported. Figure 13 shows the close agreement between frequencies estimated by these two methods.

As shown in table 1 of Strickland & Simpson (1975), the characteristic bursting frequencies from the short-time autocorrelation histogram appear to correlate with the outer-flow velocity and length scales, U_∞ and δ, as do the bursting frequencies for the zero-pressure-gradient case. However, $U_\infty/\delta n_A$ is between 11·7 and 8·35 for the present flow whereas values of about 5 are reported for the zero-pressure-gradient case (Rao, Narasimha & Badri Narayanan 1971). The inner-variable scaling $U_\tau^2/\nu n_A$ suggested by Black (1968) and Meek (1972) fails to correlate these data. It should be noted that this large-eddy scaling continues even after the boundary layer separates. Although the sensor is not directionally sensitive and the spectra in the separated region may be distorted, the autocorrelation results are not particularly sensitive to the nonlinear nature of the rectification of the signal, but reflect the repetitive nature of the signal.

The spanwise spatial structure of the sublayer was determined using the two-sensor wall unit described in §2 above. The unit was located spanwise across the tunnel with the direction of travel of the slider plate perpendicular to the streamwise direction. In addition to the long-time cross-correlation method of deducing the spanwise periodicity λ_Z from the distance between adjacent peaks, two alternative methods of signal processing to retrieve information on spatial structure were used and are described in more detail by Simpson (1975).

The correlation-frequency method (CFM) uses the relative frequency of occurrence of good short-time cross-correlations above a threshold level at a given spanwise or Z spacing. The second method, which is somewhat related,

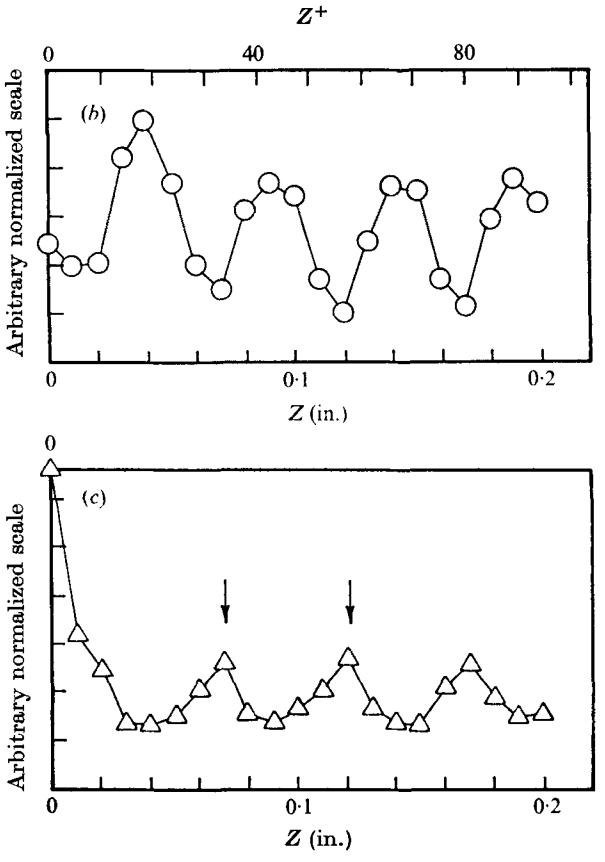

FIGURE 15. Station at 108·8 in. (*a*) Long-time spanwise correlation results. Amplitude probability distribution results: (*b*) the largest positive pulse recorded *vs.* Z; (*c*) the maximum probability value *vs.* Z; arrows denote local maxima shown in (*a*). Experimental data points connected by solid line for visual aid only.

uses the probability distribution (PD) of the product of the two sensor signals. Zero-pressure-gradient results obtained using the CFM were found to be in good agreement with previously reported measurements.

For the adverse-pressure gradient flow at the stations at 126·8, 117·8 and 108·8 in., measurements of the long-time spanwise correlation

$$s\hat{R}(Z) \equiv \left(\int_0^\infty \tau_w(0)\,\tau_w(Z)\,dt\right)\left(\int_0^\infty [\tau_w(0)]^2\,dt\right)^{-1}$$

revealed a distinct spanwise periodic behaviour superimposed on a larger-scale decay of the correlation such as that shown in figures 14 (*a*) and 15 (*a*). Evidently large-scale structures produce the high correlation level while the small-scale periodic variations are due to the sublayer behaviour. The time record over which each data point was obtained was 131·1 s. Amplitude probability distributions of the short-time correlation

$$sR(Z, T_s) \equiv \int_t^{t+T_s} \tau_w(0)\,\tau_w(Z)\,dt/T_s$$

were obtained at various Z spacings for the stations at 117·8 and 108·8 in. The sample time T_s was 0·5 ms and the total record time was 65·54 s, thus producing $1{\cdot}32 \times 10^5$ sample points.

Figure 3 of Simpson (1975) shows the qualitative behaviour of the probability distributions. At Z locations where there was a local maximum in the long-time correlation, the probability of more large amplitude positive pulses was greatest. As shown in figures 14 (*b*) and 15 (*b*) the largest amplitude positive pulse recorded seems to vary periodically with Z. The Z locations of maximum amplitude pulses also closely correspond to the Z locations of local maxima in the long-time correlations. At the same locations, the probability of more large amplitude negative pulses was found to be also slightly greater. Since the area under each probability distribution is the same, the Z locations at which the largest amplitude pulses occurred were also the locations at which low amplitude signals were least probable. Figure 14 (*c*) and 15 (*c*) show the Z variation of the maximum probability to be the mirror image of the local maximum amplitude curves shown in figures 14 (*b*) and 15 (*b*). Figure 2 of Simpson (1975) shows long-time spanwise correlations and the results from the CFM for the station at 89·7 in. The long-time correlation possesses numerous peaks with some variation in their spacing while the CFM results show a more regular spacing of peaks. There is fairly good agreement on the common location of local peaks.

The station at 139·1 in. was near the downstream end of the intermittent separation zone, where the time-averaged wall shearing stress was small and negative. The $s\hat{R}(Z)$ results indicate no distinct periodic structure while the CFM indicates a distinct correlation-frequency maximum at $Z = 0{\cdot}42$ in. and a secondary maximum at $Z = 0{\cdot}9$ in. A dip in the long-time correlation coincides with a dip in the correlation frequency at $Z = 0{\cdot}34$ in. Also, a small local maximum in $s\hat{R}(Z)$ is seen at $Z = 0{\cdot}42$ in.

The results at the stations at 156·8 and 165·8 in. were somewhat more difficult to interpret since low velocity backflow occurred at these locations. Several oscillations occurred on a weakly decaying large-scale correlation $s\hat{R}(Z)$ while the CFM showed distinct peaks occurring at about $Z = 0{\cdot}43$ in. and $Z = 1{\cdot}15$ in. Judging by the proximity of a local peak in $s\hat{R}(Z)$ at $Z = 0{\cdot}55$ in. it seems likely that $\lambda_Z \approx 0{\cdot}5$ in. Further support for this value of λ_Z is given by other local peaks in $s\hat{R}(Z)$ occurring at 1·15 in. and 1·65 in., at approximately integral multiples of λ_Z. At 165·8 in., the long-time correlation also showed peaks at approximately integral multiples of the estimated λ_Z. Table 2 is a summary of the experimental results. Values of λ_Z reported here are the distances between the first two spanwise maxima. The significance of these results is discussed in §6. The integral length scale

$$L_Z = 2\int_0^{Z_1} s\hat{R}(Z)\,dZ$$

was estimated using the long-time correlations. For the stations upstream of the separation zone, the above integral was evaluated with Z_1 the location of the minimum of the large-scale decaying correlation. Also, Z_1 seemed to be approximately $\frac{1}{2}\delta$. For the three downstream stations, the wall sensor unit could not produce sufficiently large Z spacing of the sensors. Thus L_Z was estimated by

Station (in.)	λ_Z (in.) From $s\hat{R}(Z)$	From CFM	From PD	L_Z
89·7	0·070	0·070	—	0·092
108·8	0·065	—	0·070	0·260
117·8	0·050	—	0·050	0·431
126·8	0·060	—	—	0·633
139·1	0·42	0·42	—	1·58
156·8	0·55	0·43	—	2·70
165·8	0·45	0·45	—	3·18

TABLE 2. Experimental results on the surface spanwise structure.

linearly extrapolating the decaying correlation function along the same large-scale decay slope to $Z_1 = \frac{1}{2}\delta$ and then performing the above integration. These results indicate that $L_Z \approx 0{\cdot}036\delta + 0{\cdot}0328\delta^2$, where the units are inches, or that the spanwise scale of the large-scale wall eddies increases approximately as the square of the shear-layer thickness in the adverse-pressure-gradient and separation regions. This indicates the influence of the large-scale outer flow on the wall region.

Intermittency

Because the above measurements with a flush-mounted hot film indicate the importance of the large-scale motions in this flow, measurements of the intermittency γ were made to examine the character of the turbulent/non-turbulent interface in the outer region and the average frequency of passage of the intermittent-region bulges. The intermittency was determined using smoke in the boundary layer as the marker of turbulent fluid and scattered light from this smoke at a given location as the detected signal. Owing to the large-scale mixing in the turbulent region the smoke is rapidly diffused there while smoke is carried across the turbulent/non-turbulent interface by the much slower process of molecular diffusion. Thus the smoke was assumed to be effectively confined to the turbulent regions of the flow. Fiedler & Head (1966) verified that values obtained by this method agree with those obtained by analysis of hot-wire signals.

The optical arrangement used to obtain the laser-Doppler anemometer signals reported by Simpson *et al.* (1973) was used to illuminate the smoke at the focal volume and to focus the light signal onto the photomultiplier tube's face. This arrangement allowed examination of a focal volume approximately 0·012 in. in diameter by 1·140 in. long. The signal passed from the photomultiplier tube through a Schmitt-trigger circuit which produced positive rectangular pulses when the input was above a preset discrimination level. The discrimination level was set at approximately 10 % of the peak PM-tube signal amplitude. The counter-timer determined the fraction of the time that the positive pulses were present, which is the intermittency. Owing to the steep slope of the PM output pulses, γ was not very sensitive to slightly different discriminator levels. Apparently the bulk of the smoke particles were smaller than those producing the laser-Doppler signals since near the wall $\gamma = 1$ and a continuous light signal was

obtained while only intermittent laser-Doppler signals were obtained. Preliminary data taken in a zero-pressure-gradient flow were found to be in close agreement with the data of Klebanoff (1955).

The intermittency factor γ of this turbulent/non-turbulent interface has been previously found to be well represented by the integral of the normal distribution curve:

$$\gamma = \frac{1}{(2\pi)^{\frac{1}{2}}\sigma}\int_{\xi}^{\infty} \exp\left(-\frac{\xi^2}{2\sigma^2}\right) d\xi, \tag{1}$$

where $\xi = y - \overline{Y}$, $\overline{Y}$ is the mean distance from the wall to the interface, where $\gamma = 0{\cdot}5$, and σ is the deviation from the mean. If this interface is viewed as a wavy pattern moving at approximately the free-stream velocity, then σ characterizes the amplitude of this pattern. γ distributions were obtained for each station at which H values are presented in table 1 and found to be in good agreement with (1) (Strickland & Simpson 1973). In addition to the conclusion that the intermittency distribution function is unaffected by separation, it should be noted that the distributions for γ and γ_p do not overlap, i.e. the backflow is entirely contained in turbulent fluid with $\gamma = 1$.

The results of Fiedler & Head (1966) showed that the parameters $\overline{Y}/\delta^*$ and σ/δ^* are strongly dependent on the shape factor H for values of H between 1·28 and 2·00. This dependence is quite strong as the limiting value ($H = 1{\cdot}28$) is approached as was found in the present experiments. For this flow, these parameters are well represented by the power-law curve fits to the data (Strickland & Simpson 1973)

$$\sigma/\delta^* = 0{\cdot}240(H - 1{\cdot}28)^{-0{\cdot}550}, \tag{2a}$$

$$\overline{Y}/\delta^* = 2{\cdot}75(H - 1{\cdot}28)^{-0{\cdot}369}. \tag{2b}$$

The results of Fiedler & Head (1966) also showed that the parameters $\overline{Y}/\delta^*$ and σ/δ^* were somewhat dependent on the streamwise pressure gradient. $\overline{Y}/\delta^*$ for a given value of H apparently increases with adverse pressure gradients while σ/δ^* decreases. Therefore direct comparison of results cannot be made. It can be noted however that the values obtained in the present work for $\overline{Y}/\delta^*$ as a function of H were only very slightly higher than the adverse-pressure-gradient series of Fiedler & Head. The values for σ/δ^* as a function of H, on the other hand, were approximately 30 % lower than those obtained from their adverse-pressure-gradient series. In the present work the dimensional quantities $\overline{Y}$ and δ both increased in the streamwise direction as separation was approached and achieved, the significance of which is discussed in § 6.

Measurements of the frequency with which turbulent bulges pass a fixed point were made by counting the number of pulses per unit time from the Schmitt-trigger output. All frequency measurements were made where $y = \overline{Y}$ since Bradbury (1965) and Wygnanski & Fiedler (1970), for example, have found that the maximum frequency of passage of the large-scale turbulent bulges occurs there. A serious problem with this method arises owing to the fact that several short duration pulses may occur as the probe volume enters and leaves a turbulent bulge, thus giving rise to frequencies which are perhaps an order of magnitude higher than the actual value.

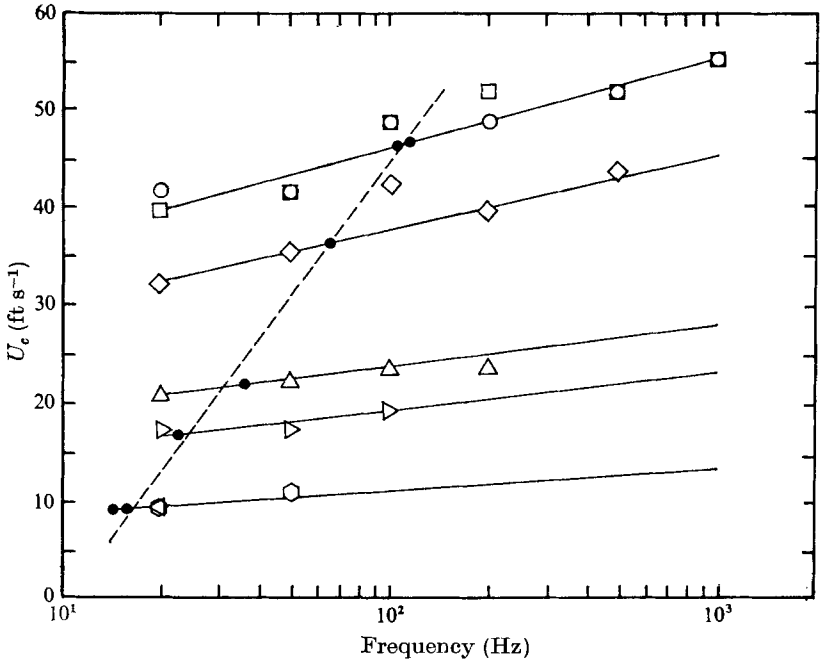

FIGURE 16. Speed of eddies measured at the wall. Stations (in.): ○, 29·2; □, 61·9; ◇, 89·9; ◁, 109·8; △, 120·2; ⬡, 131·0; ▷, 135·0. ●, bursting frequency at a given station from figure 13.

In order to reduce the effects of this problem, the signal from the Schmitt-trigger was processed through a low-pass filter which attenuated the short duration pulses responsible for the higher frequency. It was found that the resulting frequency selected was quite dependent on the filter setting, so the filter setting was obtained by visual comparison of the unfiltered PM-tube signal with the filtered Schmitt-trigger signal on a dual-trace storage oscilloscope. Typical signal and oscilloscope traces are given by Strickland & Simpson (1973). The filter was set such that there was a single zero crossing from negative to positive for each 'significant' peak on the unfiltered PM-tube signal. The low-pass filter setting chosen for all of the results shown here was 600 Hz.

These results are plotted in figure 13 along with bursting-frequency measurements. The measured intermittency frequency is approximately 55% higher than the bursting frequency. Since the technique used to obtain the intermittency frequency requires a certain amount of arbitrary judgement, it cannot be determined whether the absolute values of these measurements are accurate. However, qualitatively the trend of the data is identical to that of the bursting frequency, indicating that the large-scale motion influencing the intermittency also influences the wall bursting frequency.

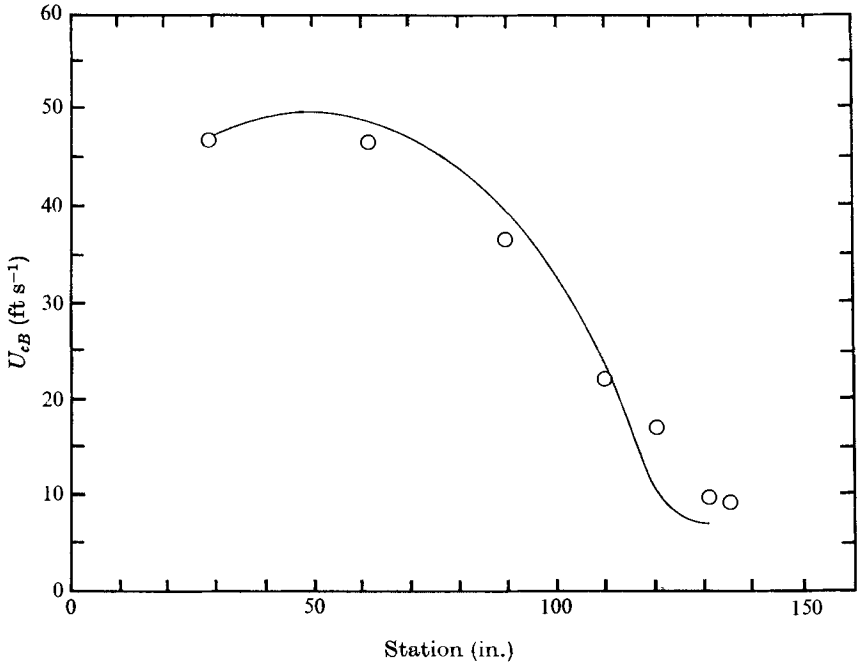

FIGURE 17. Wall speed of eddies associated with bursting ○, U_{cB}; ——, $14U_\tau$.

Eddy speed

The speed U_c of eddies of various sizes was measured at the wall as well as at several locations in the flow away from the wall to examine the effect of the strong adverse pressure gradient on this quantity. For the wall measurements two flush-mounted hot-film sensors were used and were in most cases spaced 2·0 in. apart in the streamwise direction, while in the flow away from the wall the two-sensor TSI Model 1244-10 probe was used. Before forming long-time correlations, the signals from the two sensors were each high- and low-pass filtered at each frequency at which data were obtained. The time corresponding to the correlation peak represents the time required for an eddy of given size to pass from the upstream sensor to the downstream sensor. Its speed is the distance between the sensors divided by the delay time.

Speeds measured at the wall are shown in figure 16. Uncertainties in estimating the peak of the cross-correlation curve were in general less than $\pm 7\,\%$. The bursting frequencies at the various stations are also indicated on this plot. The wall speed U_{cB} at the bursting frequency can thus be obtained from this figure. Note that the logarithm of the bursting frequency appears to be a linear function of the wall speed at the bursting frequency. In figure 17, U_{cB} is plotted as a function of streamwise location along with the quantity $14U_\tau$. U_τ was obtained using the results from the surface hot-film sensor described in §4. The agreement between the two types of data is seen to be reasonably good, particularly for larger speeds. Near separation, where $14U_\tau$ is about $30\,\%$ lower than U_{cB}, it should be recalled from §4 that the spread in the data for U_τ obtained by various methods

is of the order of $\pm 8\,\%$, the U_τ obtained from hot films being the lowest. Therefore the correlation $U_{cB}/U_\tau \approx 14$ appears to be a reasonable value in the light of the uncertainties in U_τ near separation. This is in good agreement with visual measurements obtained by Kline *et al.* (1967) for the velocities of streaks of dye ejected away from the wall and downstream by the bursting process, resulting in $U_{cB}/U_\tau \approx 13{\cdot}8$. Morrison, Bullock & Kronauer (1971) found the eddy speed in the sublayer of a fully developed turbulent pipe flow to be essentially constant with respect to frequency. Speeds obtained from their measurements ranged from $8U_\tau$ at low Reynolds numbers to $16U_\tau$ at high Reynolds numbers.

Because of the distance between the sensors, the eddies tend to dissipate in passing from one sensor to the other. This is more noticeable as the bandpass frequency is increased and as the speed decreases. Therefore eddy speeds could not be obtained at high frequencies. In fact, at the station at 135 in. the speeds of eddies with frequencies of more than 20 Hz were unobtainable. At the station at 141 in. the speed at 20 Hz was unobtainable. Since the lowest bandpass frequency obtainable with the available equipment (for two channels) was 20 Hz, the unfiltered signal was used. The unfiltered signal gave a speed which was approximately the same as the unfiltered signal at the station at 135 in. At stations downstream of this point, the time delay to the peak of the unfiltered cross-correlation was negative yet very nearly zero. The peak was broad and difficult to interpret. This suggested that in the separated region some eddies move downstream while slightly more move upstream, producing the negative time delay on the long-time cross-correlation. This result prompted a further experiment downstream.

The two-sensor wall unit was located at the station at 164·2 in. with the slider plate traversable in the streamwise direction. The time-delayed cross-correlation of the signals from these two sensors was obtained for 0·1 in. and 0·3 in. spacings. In all cases, the wide-band long-time peak correlation occurred close to zero time delay. Examination of simultaneous wide-band signal traces from the sensors on a storage oscilloscope revealed that at times recognizable characteristics occurred in one signal several milliseconds before occurring in the other and vice versa. This indicated that even that far downstream of separation some eddies were moving upstream and others downstream, or that possibly large-scale eddies were passing over both sensors almost simultaneously. Short-time correlations (0·5 s record time) indicated average upstream and downstream speeds of about 5 and 1 ft s^{-1} respectively, values which are about equal to the mean upstream and downstream flow velocities determined near the wall by the laser anemometer at that station. The significance of these results is discussed further in § 6.

Eddy speeds obtained away from the wall are given by Strickland & Simpson (1973), but are not presented here since the data behave very similarly to those given by Favre *et al.* (1967) and others for zero-pressure-gradient boundary layers. The measured speeds appear to be frequency dependent, the lower frequency (large-scale) eddies moving more slowly than the higher frequency ones. This is in contrast to Taylor's (1938) approximation, which suggests that, when the mean velocity which carries the eddies is large compared with the velocity fluctuations,

all eddies move at the local mean velocity no matter what their size. It is interesting to note that the mean velocity and unfiltered eddy speed are approximately the same, although near the wall $U_c > U$ while near the free stream $U_c < U$, as Favre *et al.* found. At the station at 156·8 in. the local mean velocity appears to become increasingly less than the unfiltered eddy speed as the region of backflow near the wall is approached.

The speed of the interface (at $\gamma = 0{\cdot}5$) of the intermittent region was determined using the laser system for illumination and smoke as a marker, as in the determination of the interfacial frequencies discussed above. The two incident laser beams were displaced streamwise 0·345 in. at their focal volumes and the scattered light from each was focused onto a separate photomultiplier tube. Cross-correlations of these signals with a long time delay provided the time required for a bulge of smoke-filled turbulent fluid to move between the laser beams. This interfacial speed U_{ci} was found to be $0{\cdot}93U_\infty$ at the station at 124·8 in. and about $0{\cdot}9U_\infty$ at 136·1 in. with about $\pm 5\,\%$ uncertainty in the measured time delay. Kovasznay, Kibens & Blackwelder (1970) found U_{ci} to be about $0{\cdot}93U_\infty$ for a flat-plate boundary layer while Wygnanski & Fiedler (1970) found U_{ci} to be about $0{\cdot}85U_\infty$ for a mixing layer. The sparse data presented here seem to be consistent with the idea that the outer part of a separating boundary layer behaves more and more like a mixing layer downstream.

The data near the wall, where $U < U_c$ ($y/\delta < 0{\cdot}3$), indicate that the large-scale eddies at the bursting frequency move at about the same speed as is measured at the wall. When $U > U_c$, the speed of the large eddies becomes progressively greater. In the limit as the intermittent region is approached, the large-scale eddies move at the interfacial speed U_{ci}.

6. Discussion

The Bradshaw, Ferriss & Atwell (1974) computer program was used to predict the behaviour of this boundary layer. Velocity and shear-stress profiles at the station at 28 in. were input. The effects of the side-wall boundary layers on the convergence were accounted for, but there was a difference of much less than 1 % when this effect was ignored. The surface shear-stress distribution (shown in figure 12) indicates very good agreement up to the station at 108 in. with the results from the flush-mounted sensor while the mean velocity profiles are in good agreement only up to about 70 in. Because of the good agreement up to this streamwise location, the discussion here will be limited to the downstream region.

Perry & Schofield (1973) have recently proposed a correlation for mean velocity profiles in unseparated flow in the presence of strong adverse pressure gradients, based upon 145 mean velocity profiles taken from Coles & Hirst (1969) and including both equilibrium and non-equilibrium profiles. This correlation applies only when the maximum shearing stress $U_M^2 = (-\overline{uv})_{\max}$ exceeds $\frac{3}{2}U_\tau^2$, where U_τ is the wall shear velocity. In the present results, only the stations at 103·8 and 124·3 in., which have negative d^2P/dx^2 values, meet this requirement. Perry & Schofield proposed that the outer flow be described by

$$(U_\infty - U)/U_s = f_2(\eta_2), \quad \eta_2 = y/\Delta, \tag{3}$$

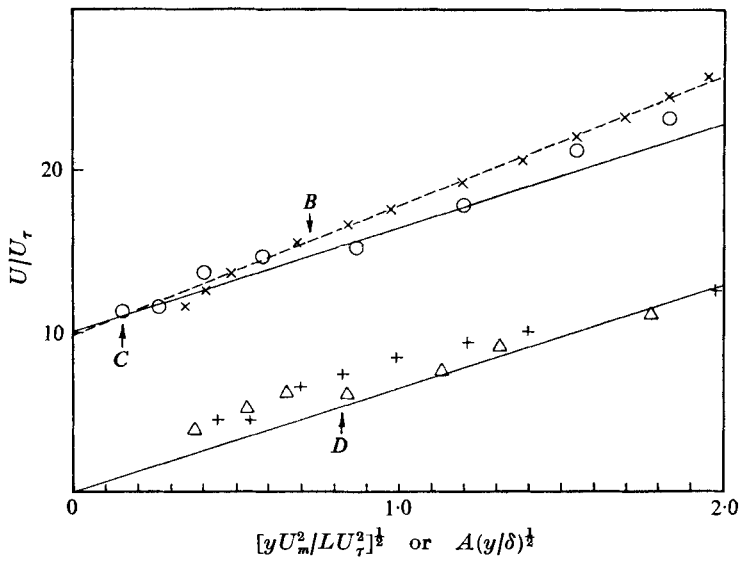

FIGURE 18. Half-power mean velocity profile relationship near the wall upstream of separation. Station at 103·8 in.: ×, hot film; ○, laser anemometer; $A = 2{\cdot}96$; B, predicted point of tangency y_c; C, $y^+ = 32$. Station at 124·3 in.: +, hot film; △, laser anemometer; $A = 8{\cdot}56$; D, $y^+ = 10$. ——, 6·4 slope; – – –, 8·05 slope.

where $f_2(\eta_2)$ is a universal function, $f_2(0) = 1$ defines the velocity scale U_s, and Δ is determined through the displacement-thickness (δ^*) integral:

$$\Delta = 2{\cdot}86\delta^* U_\infty / U_s. \tag{4}$$

Nearer the wall

$$\frac{U}{U_\tau} - h = f_1(\eta_1), \quad \eta_1 = \frac{y}{e}, \quad e = \frac{LU_\tau^2}{U_M^2}, \tag{5}$$

where h is a function of $U_M^2 \nu / LU_\tau^3$ and L is the distance from the wall to the maximum in the local shear-stress profile. The proposed relation for e was determined empirically. The existence of an overlap region between f_1 and f_2 requires that in that region

$$f(\eta_1) = 6{\cdot}4\eta_1^{\frac{1}{2}} \tag{6}$$

and that

$$U_s/U_M = 8{\cdot}0\,(\Delta/L)^{\frac{1}{2}}, \tag{7}$$

where the constants were determined empirically.

Within the inner flow nearest the wall, (5) takes the usual logarithmic form for $yU_\tau/\nu > 30$, i.e.

$$\frac{U}{U_\tau} = \frac{1}{0{\cdot}41} \ln \left| \frac{yU_\tau}{\nu} \right| + 5{\cdot}0, \tag{8}$$

and $U^+ = y^+$ in the viscous sublayer. The point where (5) and (8) match is

$$y_c = 0{\cdot}58e \quad \text{or} \quad y_c/\Delta = 37{\cdot}1U_\tau^2/U_s^2. \tag{9}$$

For the data presented here U_s/U_∞ was determined from a U/U_∞ *vs.* $(y/\delta)^{\frac{1}{2}}$ plot with the slope of the half-power region extrapolated to the wall, as suggested by

Station ...	103·8 in.	124·3 in.
U_s/U_∞	0·7	0·96
U_s/U_M	17·64	17·38
U_s/U_{Mp}	16·7	15·74
y_c/Δ	0·0606	0·00453
Δ/δ	1·01	1·29
L/δ	0·25	0·45

TABLE 3. Experimentally determined parameters for the Perry & Schofield correlation.

Perry & Schofield. This and other parameters are shown in table 3. In terms of U/U_∞ *vs.* y/δ, the centre of the band of data presented in figure 6(*a*) of Perry & Schofield for $f_2(\eta_2)$ is plotted on figure 4. For the station at 103·8 in. there is very good agreement with the measurements and the scatter is well within the scatter of their correlation. For the station at 124·3 in. there is more deviation but the present results fall along the edge of the scatter in their correlation.

Nearer the wall there is some scatter in the present results, as shown in figure 18, but (5) and (6) seem to be roughly satisfied. At the station at 103·8 in. the slope of (6) seems to be followed by the laser results while the hot-film results require a slope of about 8·05. The predicted matching point y_c is substantially further out in the boundary layer than the inner edge of the logarithmic region. At the station at 124·3 in. the predicted matching point occurs in the sublayer, so supposedly no logarithmic region remains. However, it should be recalled from §4 that good agreement between wall shear-stress measurements that do and do not require the assumption of a logarithmic law of the wall seems to support the existence of some logarithmic region at this station. Plots of U/U_τ *vs.* yU_τ/ν (Simpson *et al.* 1973) also support (8) near the wall at these two locations. Figure 5 shows a logarithmic region for the station at 124·3 in. for $y/\delta < 0{\cdot}01$. When $U_\tau \to 0$, $h \to 0$ and (5) and (6) should become independent of U_τ. Possibly this condition is being approached at the station at 124·3 in.

The experimentally determined values of U_s/U_M and Δ/L fall within the scatter of the plot from which Perry & Schofield obtained (7). However, better agreement with (7) is obtained if the 'pseudo-shearing stress'

$$U_{Mp}^2 = \left(-\overline{uv} + \int_y^\infty \frac{\partial(\overline{u^2} - \overline{v^2})}{\partial x}\, dy \right)_{\max} \tag{10}$$

is used for the maximum shear. x derivatives were estimated using the similarity of the $\overline{u^2} - \overline{v^2}$ profile along the flow (Simpson *et al.* 1974). Curves showing this quantity are given in figure 10. The reason for using it is that Perry & Schofield neglected the normal-stress term in the momentum equation

$$U\frac{\partial U}{\partial x} + V\frac{\partial U}{\partial y} + \frac{1}{\rho}\frac{dP_\infty}{dx} = \frac{\partial}{\partial y}\left(\frac{\tau}{\rho} + \int_y^\infty \frac{\partial(\overline{u^2} - \overline{v^2})}{\partial x}\, dy \right) \tag{11}$$

when they used this equation to produce shear-stress profiles from mean velocity profiles. Consequently they were effectively calculating U_{Mp}^2.

The data analysis of Perry & Schofield did not support the mixing-length theories (Townsend 1962; McDonald 1969) which predict a significant departure of the velocity profile from (8) under strong adverse pressure gradients. The present results do not support them either. These theories are based on a linear shearing-stress distribution near the wall which is a function of pressure gradient while ignoring the normal-stress and convective terms. For the station at 124·3 in., the present data suggest that at $y/\delta \approx 0{\cdot}05$

$$\frac{\partial(-\overline{uv}/U_\infty^2)}{\partial(y/\delta)} \approx 2\times 10^{-3} \quad \text{while} \quad \frac{\delta\,\partial(\overline{u^2}-\overline{v^2})}{U_\infty^2\,\partial x} \approx 5\times 10^{-4},$$

so that near separation normal-stress terms near the wall are quite significant in the momentum equation compared with the shear term. Also note that, while the $-\overline{uv}$ measurements near the wall are relatively uncertain, τ seems to be fairly independent of y and agrees with the wall value, an observation consistent with other measured $-\overline{uv}$ data (Newman 1951).

The recent results of Samuel & Joubert (1974) also mainly support this picture. They found that the law of the wall held all along their adverse-pressure-gradient flow, but with the constants 0·40 and 5·1 instead of those given in (8). Distinct half-power regions were found outside and overlapping the logarithmic region when U_M^2 exceeded $\frac{3}{2}U_\tau^2$, which occurred when d^2P/dx^2 was negative. Equation (3) was closely satisfied by their mean velocity profile data, while (6) and (7) were satisfied with the constants replaced by 10 and 12·5 respectively. Since the latter two equations incorporate values of L and U_M obtained from the shearing-stress distribution, it appears that the differences arise from this source. Samuel & Joubert also found that the convective terms of (11) offset the pressure-gradient term near the wall when d^2P/dx^2 was positive, so that the shear-stress gradient there was approximately zero. On the basis of all these data it is safe to say that the law of the wall holds all along an adverse-pressure-gradient flow and that the convective and normal-stress terms of the momentum equation are significant near the wall and make the shear-stress gradient less than the streamwise pressure gradient. Furthermore, when U_M^2 exceeds $\frac{3}{2}U_\tau^2$ a universal outer region scaled on Δ and U_s exists and a half-power velocity profile exists just outside and overlaps the logarithmic region.

For the present data the characteristic wall bursting frequency scaled best on the outer variables and was proportional to the bulge passage frequency of the intermittent region. The eddy speed at the wall at the bursting frequency was about the same as for zero-pressure-gradient flows, being proportional to U_τ. These results are not surprising since the law of the wall was seen to hold here and the same behaviour is observed for zero-pressure-gradient flows where the law of the wall holds. However, $U_\infty/\delta n_A$ increases from about 10 to about 13·5 at the station at 89 in., which is 25 in. downstream of where free-stream deceleration begins and about 7 in. upstream of the maximum pressure gradient. $U_\infty/\delta n_A$ decreases downstream as separation is approached and realized. Naturally, this variation is due to the pressure-gradient distribution along the flow.

As one can see from table 2, λ_Z is approximately constant while U_τ strongly decreases as separation is approached, making $\lambda_Z^+ = \lambda_Z U_\tau/\nu$ also strongly de-

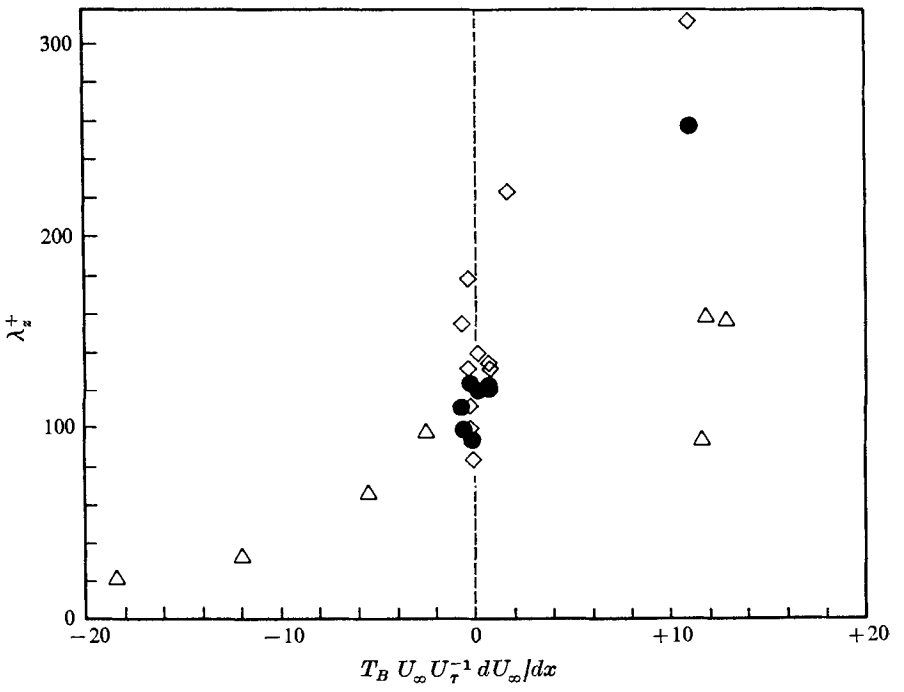

FIGURE 19. Variations of λ_z^+ with pressure gradient: ●, visual results of Kline *et al.* (1967); ◇, correlation results of Kline *et al.* (1967); △, present results.

crease. Figure 19 shows λ_Z^+ as a function of the dimensionless pressure-gradient parameter. A plausibility argument can be put forward for the characteristic dimensionless parameter used here which makes the spread in observed λ_Z^+ values with pressure gradient plausible. The speed of the wall eddies is approximately proportional to U_τ, so that $U_\tau T_B$, where T_B is the bursting period $1/n_A$, is proportional to the average streamwise spacing of these eddies. The ratio of the stresses acting in the wall region should also influence the spanwise structure, so that $\tau_w^{-1}\, dP_\infty/dx$ is the ratio of these stresses per unit length. Thus

$$\frac{-U_\tau T_B}{\tau_w}\frac{dP_\infty}{dx} \quad \text{or} \quad \frac{T_B U_\infty}{U_\tau}\frac{dU_\infty}{dx} = P_T$$

constitutes a non-dimensional parameter describing the relative influence of the pressure gradient and the wall shear on each eddy which passes by. For $x > 89$ in., the pressure gradient plays an increasing role as λ_Z^+ decreases from its zero-pressure-gradient value of about 100 with increasingly negative values of P_T. After separation, λ_Z increases by almost an order of magnitude and the backflow near the wall is subjected to a weak favourable pressure gradient since dU_∞/dx is still negative. These λ_Z^+ values are shown for a positive P_T and take on magnitudes near 100. The uncertainty in the mean wall shear values and the pressure gradient may be relatively large at these latter stations, contributing to some uncertainty in λ_Z^+ and P_T.

Also shown on figure 19 are the λ_Z^+ results of Kline *et al.* (1967), which are the

only other published results available for flows with a non-zero pressure gradient. With exception of the results for strongly accelerating flow, most of their data were obtained at low P_T values. Although there is considerable scatter in their results, a curve passing through the few data points from the present investigation for $P_T < 0$ would intersect the centre of their data at $P_T = 0$. In terms of the pressure-gradient parameter $K = (\nu dU_\infty/dx)\, U_\infty^{-2}$, the data for their flow with a strong adverse pressure gradient had values of the order of -10^{-6} while the present data had values of about -2×10^{-7}. Thus one cannot see any trend of the influence of pressure gradient using this parameter. While their mean velocity profiles matched the outer-region correlation of Perry & Schofield, no shear-stress profiles were available for examination. Their momentum-thickness Reynolds number was an order of magnitude smaller than for the present flow; $\frac{1}{2}C_f$ was about twice as large so their flow was not near separation. Thus P_T seems to be one parameter which permits a monotonic variation of λ_Z^+ with pressure gradient. It should be noted that if one scales λ_Z on U_M, which we have observed to be an important velocity scale near separation, then $\lambda_Z U_M/\nu$ has a value of about 115 at the station at 103 in. and a value of about 109 at the station at 124 in. This suggests that the maximum shearing stress should be used to non-dimensionalize λ_Z, making $\lambda_Z U_M/\nu$ a more general parameter for the wall spanwise structure upstream of separation with a value of about 100.

The description of turbulent boundary-layer separation is not clear cut as in a steady laminar flow, where separation is presumed to occur at a location along the flow where the wall shear vanishes. Turbulent separation, or intermittent separation according to Sandborn & Kline (1961), occurs at the upstream point at the wall where backflow begins on an *intermittent* basis. This point is the intermittent separation point or the *turbulent separation point*. Downstream of this location γ_p decreases along the wall in the *intermittent separation region*, where flow moves both upstream and downstream on an intermittent basis. The so-called *fully developed separation point* or time-averaged separation point is where the average wall shear stress is zero.

It is clear from figure 6 that intermittent separation begins somewhere downstream of the station at 120 in. At the station at 124 in., $\gamma_p \approx 0{\cdot}8$ near the wall, which, as pointed out in § 4, appears to be about the lowest value of γ_p for which the hot-film mean velocity values are not appreciably affected by signal rectification. This would be a good criterion for the beginning of intermittent separation, considering also the uncertainty in measuring γ_p as noted in figure 6. Figures 2 and 3 indicate that the pressure gradient drops off rapidly after intermittent separation, which seems reasonable since intermittent pressure-gradient relief would follow intermittent flow detachment from the wall.

Figure 20 presents the separation criteria of Sandborn as discussed by Sandborn & Kline (1961), which are based on examination of many laminar and turbulent separation velocity profiles. For intermittent separation they proposed the relation

$$H = 1 + (1 - \delta^*/\delta_{0{\cdot}995})^{-1}, \tag{12}$$

while the laminar velocity profile at zero wall shear was proposed to predict the H *vs.* $\delta^*/\delta_{0{\cdot}995}$ curve on which fully developed separation was located. The present

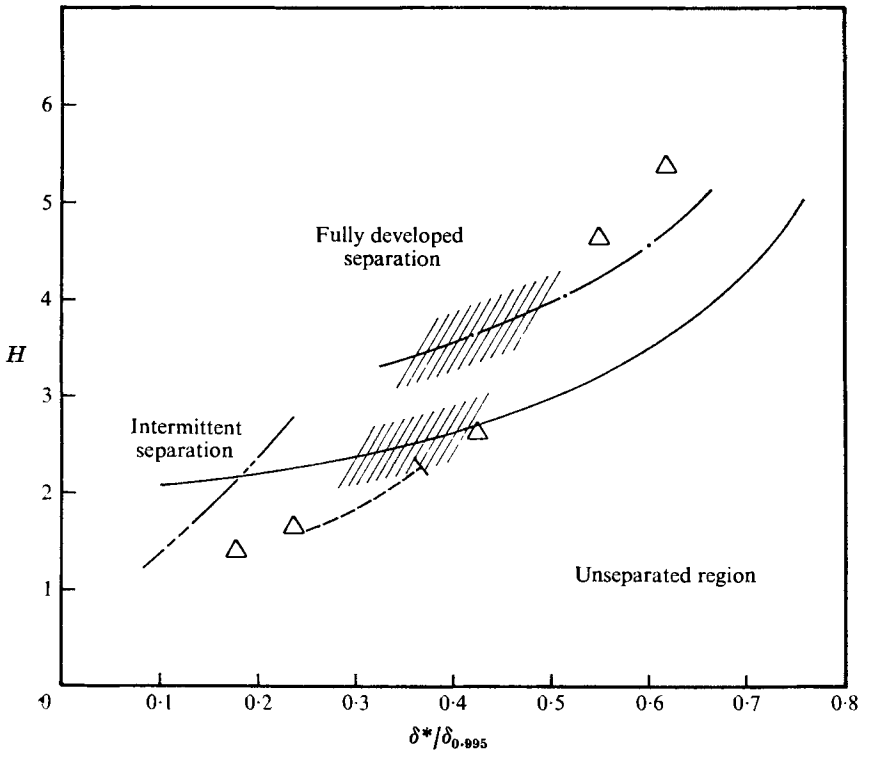

FIGURE 20. H *vs.* $\delta^*/\delta_{0.995}$. △, present data at 88·2, 103·8, 124·3, 139·1 and 157·1 in. respectively, for increasing H; ▨, data for intermittent and fully developed separation (Sandborn & Kline 1961); – – –, path predicted from Perry & Schofield velocity profiles; ——, intermittent separation; —·—, fully developed separation (Sandborn); — — — —, data of Sandborn & Liu (1968).

data are in good agreement with these criteria. Although no velocity profile data were taken at the station at 132 in., interpolating between the 124·3 in. and the 139·1 in. data points on figure 20 places 132 in. somewhere near the fully developed separation curve. The data of Sandborn & Liu (1968), which agree with these criteria, indicated that $\gamma_p \approx 0{\cdot}7$ near the wall at intermittent separation, in fair agreement with the above proposal that $\gamma_p \approx 0{\cdot}8$ at intermittent separation.

Use of the Perry & Schofield correlation implies that there is only one H *vs.* $\delta^*/\delta_{0.995}$ path that a flow can follow to separation. This is implied by (3), which can be manipulated using their $f_2(n_2)$ correlation plot to produce the curve shown on figure 20 for this path. If one allows $U_S \rightarrow U_\infty$, which implies that the half-power relation approaches the wall, then $U_\tau \rightarrow 0$ and separation is predicted at $H = 2{\cdot}28$. Judging by all these data and figure 20 it can only be the intermittent separation, although this prediction is only fair. The data used by Perry & Schofield were obtained from flows over flat or low-curvature faired surfaces as were the data presented here. The data of Sandborn & Liu were obtained after a moderately large change in curvature. The H *vs.* $\delta^*/\delta_{0.995}$ path for their data was at considerably lower $\delta^*/\delta_{0.995}$ than that for data presented here or by Perry &

Schofield. Evidently the surface curvature is important in determining this path, and the Sandborn criteria are thus more general.

Downstream of separation the outer-region mean velocity profiles behave similarly to a two-dimensional mixing layer. For $U/U_\infty > 0{\cdot}3$ the equation presented by Strickland & Simpson (1973),

$$\frac{U-U_0}{U_\infty-U_0} = \frac{1}{2}\left[1+\operatorname{erf}\left(\frac{\delta' y'}{x'}\right)\right], \tag{13}$$

was found to fit the mean velocity profiles, where $\delta' = 35$, $U_0/U_\infty = 0{\cdot}2$, y' is measured from $U/U_\infty = 0{\cdot}6$, near the maximum shear location, and x' is measured from 88 in. As shown on figure 4 this relation does not fit the data at 124·3 in. very well. The value of δ' is about twice the value obtained for mixing layers with zero pressure gradient and with $U_0/U_\infty = 0{\cdot}2$ (Halleen 1964). The intermittency results presented here and those of Fiedler & Head (1966) show that $\overline{Y}$ and σ both increase with streamwise distance along a separating boundary layer. Fiedler & Head stated in their conclusions that σ decreased with distance, but their figure 12 showed that, for $H > 2$, $\sigma/\overline{Y}$ was about constant. Hence, since their $\overline{Y}$ rapidly increased with distance, so too must their σ. The significance of this is that the intermittent region of a separating boundary layer grows in width. Their conclusion that the structure of the intermittent region of a separating boundary layer does not approach that of a free wake or mixing layer, with its wide intermittent region, is not supported by their measurements or those presented here. The sparse data presented here for the interfacial speed of the intermittent region also indicate that the outer part of this separating boundary layer behaves more and more like a mixing layer. The spanwise integral scale L_Z grows faster than δ, so that at the station at 165·8 in. L_Z/δ is greater than 0·3, which indicates that a progressively larger eddy structure is evolving and is imposing itself on the wall-region flow.

Rather flat mean velocity profiles are observed for $y/\delta < 0{\cdot}15$ downstream of the beginning of intermittent separation. In the same region the γ_p profile is fairly flat, as seen in figure 7, as are the average positive and average negative velocities (Simpson *et al.* 1974). The surface hot-film results also indicated that some eddies were moving upstream while others moved downstream. The surface shearing stress is quite low compared with the stresses measured in the outer region. In essence, it appears that the region is quite passive with very little momentum or mean kinetic energy as compared with the outer region. It does not seem conceivable that the flow in this region could strongly control the outer-region flow. On the contrary, the outer-region flow, with its relatively high momentum, kinetic energy and shearing stress should control the wall region. This low velocity region evidently merely serves the purpose of providing just the small amount of net backflow required to satisfy continuity after the energetic flow near the free stream has deflected away from the wall upon separation.

Figure 8 strongly suggests that there is some flow-field similarity downstream of separation, the maximum streamwise r.m.s. fluctuation $(\overline{u^2})^{\frac{1}{2}}_{\max}$ and the distance M from the wall to the location of this maximum being the velocity and length scales respectively. Figure 4 indicates that the location of maximum $\overline{u^2}$

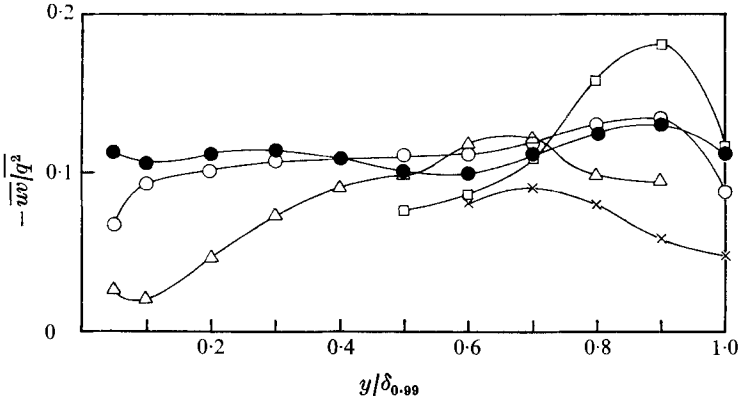

FIGURE 21. $-\overline{uv}/\overline{q^2}$ distributions at the various stations (in.): ●, 88·2; ○, 103·8; △, 124·3; □, 139·1; ×, 157·1.

occurs at $U/U_\infty \approx 0{\cdot}5$ for the stations at 139·1 and 157·1 in. while the mean velocity changes direction at $y/M \approx 0{\cdot}25$. The velocity profile similarity equation (13) also indicates mean velocity profile similarity, at least in the outer region, γ_p provides further evidence.

The data shown in figure 7 were replotted to test the proposed similarity relation

$$(\gamma_p - \gamma_{p0})/(1-\gamma_{p0}) = g(y/M), \tag{14}$$

where γ_{p0} is the near-wall value shown in figure 6. For stations downstream of intermittent separation, (14) was satisfied to within about $\pm 0{\cdot}05$ at a given y/M. An empirical curve fit, accounting for the linear portion and the tail near $y/M = 1$, produces

$$g(y/M) = 1{\cdot}58(y/M - 0{\cdot}08) - 0{\cdot}453\exp(-27{\cdot}1(1-y/M)^2), \quad 0{\cdot}1 < y/M \leqslant 1. \tag{15}$$

Thus the apparent similarity of the separated flow field is supported by all the data presented here.

The turbulence structure seems representative of previous adverse-pressure-gradient work, although the effects of the normal-stress terms have not previously been emphasized. Figure 21 is a plot of $-\overline{uv}/\overline{q^2} = a_1$ for the various stations. This parameter represents the fact that in most flows the turbulence energy is a direct result of shear production. Bradshaw (1967*a*) obtained values of a_1 around 0·15 for two equilibrium-type adverse-pressure-gradient flows, with values as low as 0·1 for small values of y/δ. Upstream, at the stations at 88·2 and 103·8 in., a_1 has a value of about 0·13 near the outer edge of the boundary layer and smaller values closer to the wall, in fair agreement with Bradshaw's result. At the station at 124·3 in., a_1 is substantially smaller near the wall, indicating either too low $-\overline{uv}$ measurements or some other source of turbulence production.

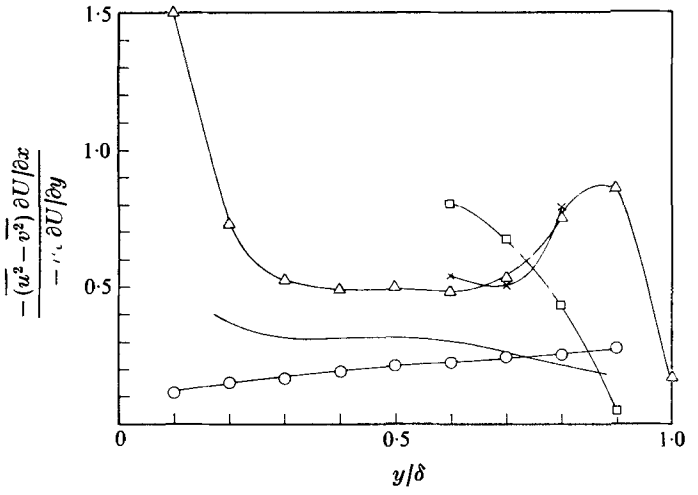

FIGURE 22. Ratio of normal-stress production to shear-stress production at the various streamwise locations (in.): ○, 103·8; △, 124·3; □, 139·1; ×, 157·1. Solid line shows results of Schubauer & Klebanoff flow near separation, at 24·5 ft.

The normal-stress production term is not negligible in the turbulence energy equation

$$\left(\frac{U}{2}\frac{\partial q^2}{\partial x}+\frac{V}{2}\frac{\partial \overline{q^2}}{\partial y}\right)+\frac{\partial}{\partial y}\left(\frac{\overline{pv}}{\rho}+\tfrac{1}{2}\overline{q^2 v}\right)+\epsilon=-\overline{uv}\frac{\partial U}{\partial y}-(\overline{u^2}-\overline{v^2})\frac{\partial U}{\partial x}, \tag{16}$$

where the terms represent advection, diffusion, dissipation, shear production and normal-stress production respectively. (The curvature turbulence production term $-\overline{uv}\,\partial V/\partial x$ (Bradshaw 1973) has been omitted from the right-side of (16), since in this flow the largest value of $(\partial V/\partial x)/(\partial U/\partial y)$ is crudely estimated to be less than 0·03. Thus the production attributable to curvature is negligibly small compared with shear production.) Figure 22 shows estimates of the ratio of normal-stress to shear production for the various stations, along with the results of Schubauer & Klebanoff (1951) near separation. If we multiply a_1 by the factor

$$F=1-\frac{(\overline{u^2}-\overline{v^2})\,\partial U/\partial x}{-\overline{uv}\,\partial U/\partial y}, \tag{17}$$

which is the ratio of total production to shear production, then $a_1 F$ should represent the ratio of the total turbulence which would be produced by the production mechanism to the turbulence energy actually produced. As separation is approached F takes on values of the order of 1·5 or 2, although uncertainties in estimating $\partial U/\partial x$ make the values in figure 22 also uncertain, especially at high and low y/δ. Clearly, though, the large value of F near the wall at the station at 124·3 in. is needed to account at least partially for the small a_1 observed. In general $a_1 F$ takes on values closer to 0·15 than a_1. This suggests that $a_1 F = 0{\cdot}15$ is a more general correlation.

Figure 11 shows that the dissipation length defined with $-\overline{uv}$ is also quite a bit lower than Bradshaw's distribution. It should be noted that the data seem to depart from the $L_\epsilon/\delta = 0{\cdot}4(y/\delta)$ relation in the vicinity of the y_c/δ predicted from

the Perry & Schofield correlation at $y/\delta \approx 0{\cdot}06$ for the station at 103·8 in. Again, $-\overline{uv}F$ should be used to represent the amount of energy available for dissipation since we have found that $a_1 F \approx 0{\cdot}15$, i.e. it seems that we should use

$$L_\epsilon/\delta = (-\overline{uv})^{\frac{3}{2}} F^{\frac{3}{2}}/\epsilon\delta \tag{18}$$

with Bradshaw's L_ϵ/δ *vs.* y/δ distribution for the left side. As shown in figure 11 the level of L_ϵ/δ using $-\overline{uv}F$ at the station at 124·3 in. is about double the result using only $-\overline{uv}$, but is still quite a bit lower than Bradshaw's distribution. At the station at 103·8 in. the result is about 30 % higher than that obtained not using F. For $y/\delta > 0{\cdot}4$, the L_ϵ/δ results using $-\overline{uv}F$ at these two stations agree with the results at the station at 88·2 in., where F is close to unity.

The entrainment velocity V_e, which is proportional to the diffusion of turbulence energy at the outer edge of the flow, was computed using the relation

$$V_e = d[U_\infty(\delta_{0{\cdot}995} - \delta^*)]/dx. \tag{19}$$

Bradshaw *et al.* (1967) found that V_e could be correlated by the maximum intensity of the Reynolds shearing stress in equilibrium as well as non-equilibrium boundary layers and at the high velocity edge of mixing layers:

$$V_e/\Delta U_1 = 10\,(-\overline{uv}_{\max}/\Delta U_1^2), \tag{20}$$

where ΔU_1 is the maximum local change in mean velocity across the layer. Results obtained using (20) were in general about 15 % higher than those computed from (19) (Simpson *et al.* 1974). The deviations are within the scatter of data originally used to obtain (20). Apparently the normal-stress production of turbulence energy does not appreciably affect the entrainment process.

7. Conclusions

The following major observations and conclusions may be drawn from the present experiments:

(*a*) For the first time laser anemometer measurements of $\overline{u^2}$, U and the fraction of the time γ_p that the flow moves downstream obtained using a directionally sensitive system are presented for a flow with an airfoil-type pressure gradient in the vicinity of separation.

(*b*) The correlations of Perry & Schofield (1973) for mean velocity profiles subjected to adverse pressure gradients are supported within the uncertainty of the data. The law of the wall appears to be valid up to intermittent separation.

(*c*) The separation criteria of Sandborn are supported, intermittent separation apparently beginning when $\gamma_p \approx 0{\cdot}8$ and the free-stream pressure gradient drops rapidly.

(*d*) Near separation the neglect of the normal-stress terms in the momentum and turbulence energy equations is not justified. As much as one-third of the turbulence energy production is attributable to these stresses. The ratio F of total turbulence energy production to shear-stress production can be used to account for these normal-stress effects on $-\overline{uv}/\overline{q^2}$ and L. There is no apparent effect on the entrainment rate.

(*e*) The separated flow field shows some similarity in $\overline{u^2}$, U and γ_p, the maximum fluctuation $(\overline{u^2})^{\frac{1}{2}}_{\max}$ and M, the distance from the wall to the maximum, being the velocity and length scales. It behaves more and more like a free shear mixing layer with the accompanying large-scale intermittent region, antisymmetric mean velocity profiles and large-scale spanwise structures. The intermittent backflow is always contained within the turbulent fluid. The net low velocity backflow apparently just serves to satisfy continuity requirements.

(*f*) The structure near the wall was found to be substantially different from that observed for the zero-pressure-gradient case. The wall bursting frequency n_A and turbulent/non-turbulent interfacial frequency were proportional and scaled on U_∞ and δ, but with $U_\infty/\delta n_A$ twice that for the zero-pressure-gradient case. $\lambda_z U_M/\nu$, where $U_M = (-\overline{uv})^{\frac{1}{2}}_{\max}$, seems to be a more general parameter for the wall spanwise structure, having a value of about 100, upstream of separation.

The authors express appreciation to Mr J. O. Hornkohl of ARO, Inc., for providing information on the construction of the Bragg cell, to Mr Ed Mauldin of NASA Langley Research Center for the impedance matching circuit design, and to Applied University Research, Inc. Dallas, Texas, for use of the prototype Model 101 Selective Signal Sampling System for the pulse shaping and sample-and-hold circuits. Initial development of the laser anemometer system was sponsored under NASA Grant NGL 44-007-006. This work was supported by the U.S. Army Research Office, Durham, under Grants DA-ARO-D-31-124-72-G31 and DAH CO4-74-G-0024. Portions of this work were presented at the NATO–AGARD Symposium on Flow Separation, 27–30 May 1975, at Göttingen, West Germany. The final draft of this paper was prepared while R.L.S. was a Visiting Professor at the Max-Planck-Institut für Strömungsforschung, Göttingen.

REFERENCES

Bakewell, H. P. & Lumley, J. L. 1967 *Phys. Fluids*, **10**, 1880.

Black, T. J. 1968 *N.A.S.A. Current Rep.* CR-888.

Bradbury, L. J. S. 1965 *J. Fluid Mech.* **23**, 31–64.

Bradshaw, P. 1967*a* *J. Fluid Mech.* **29**, 625–645.

Bradshaw, P. 1967*b* *Nat. Phys. Lab. Aero. Rep.* no. 1220.

Bradshaw, P. 1973 *AGARD Rep.* AGARD-AG-169.

Bradshaw, P., Ferriss, D. H. & Atwell, N. P. 1967 *J. Fluid Mech.* **28**, 593–616.

Bradshaw, P., Ferriss, D. H. & Atwell, N. P. 1974 *Imperial College Aero. Rep.* no. 74–02 (revised version of Bradshaw *et al.* (1967) with K. Unsworth).

Brodkey, R. S., Hershey, H. C. & Corino, E. R. 1969 *Symp. Turbulence in Liquids, Univ. Missouri-Rolla* (ed. J. L. Zakin & G. Patterson), p. 129.

Champagne, F. & Sleicher, C. A. 1967 *J. Fluid Mech.* **28**, 177–182.

Coles, D. & Hirst, E. 1969 *Comp. Turbulent Boundary Layers.* 1968 *AFOSR–IFP Stanford Conf.*, vol. 2. *Data Compilation.*

Collins, M. A. & Simpson, R. L. 1976 *Dept. Civil Engng, Southern Methodist Univ., Rep.* WR–4.

Corino, E. R. & Brodkey, R. S. 1969 *J. Fluid Mech.* **37**, 1–30.

Echols, W. H. & Young, J. A. 1963 *Naval Res. Lab. Rep.* no. 5929.

FIEDLER, H. & HEAD, M. R. 1966 *J. Fluid Mech.* **25**, 719–735.

FREYMUTH, P. 1967 *Rev. Sci. Inst.* **38**, 677–681.

GUPTA, A. K., LAUFER, J. & KAPLAN, R. E. 1971 *J. Fluid Mech.* **50**, 493–512.

HALLEEN, R. M. 1964 *Thermosci. Div., Dept. Mech. Engng., Stanford Univ., Rep.* MD-11.

KIM, H. T., KLINE, S. J. & REYNOLDS, W. C. 1971 *J. Fluid Mech.* **50**, 133–160.

KLEBANOFF, P. 1955 *N.A.C.A. Rep.* no. 1247.

KLINE, S. J. & MCCLINTOCK, F. A. 1953 *Mech. Engng*, **75**, 3–8.

KLINE, S. J., REYNOLDS, W. C., SCHRAUB, F. A. & RUNSTADLER, P. W. 1967 *J. Fluid Mech.* **30**, 741–773.

KOVASZNAY, L. S. G., KIBENS, V. & BLACKWELDER, R. E. 1970 *J. Fluid Mech.* **41**, 238–325.

MCDONALD, H. 1969 *J. Fluid Mech.* **35**, 311–336.

MAZUMDER, M. K., HOYLE, B. D. & KIRSCH, K. J. 1974 *Proc. 2nd Int. Workshop Laser Velocimetry*, vol. 2 (ed. H. D. Thompson and W. H. Stevenson), pp. 234–269. Purdue Univ. School Mech. Engng.

MEEK, R. L. 1972 *A.I.Ch.E. J.* **18**, 854–855.

MORRISON, W. R. B., BULLOCK, K. J. & KRONAUER, R. E. 1971 *J. Fluid Mech.* **47**, 639–656.

NEWMAN, B. G. 1951 *Dept. Supply Aero. Res. Consultative Comm., Univ. of Sydney, Rep.* ACA-53.

PERRY, A. E. & SCHOFIELD, W. H. 1973 *Phys. Fluids*, **16**, 2068–2074.

RAO, K. N., NARASIMHA, R. & BADRI NARAYANAN, M. A. 1971 *J. Fluid Mech.* **48**, 339–352.

ROTTA, J. C. 1962 *Progress in Aeronautical Sciences*, vol. 2, pp. 1–219. Pergamon.

SAMUEL, A. E. & JOUBERT, P. N. 1974 *J. Fluid Mech.* **66**, 481–505.

SANDBORN, V. A. & KLINE, S. J. 1961 *J. Basic Engng, Trans. A.S.M.E.* **83**, 317–327.

SANDBORN, V. A. & LIU, C. Y. 1968 *J. Fluid Mech.* **32**, 293–304.

SCHUBAUER, G. B. & KLEBANOFF, P. S. 1951 *N.A.C.A. Rep.* no. 1030.

SIMPSON, R. L. 1975 *Phys. Fluids*, **18**, 1068–1069.

SIMPSON, R. L. 1976 *A.I.A.A. J.* **14**, 124–126.

SIMPSON, R. L. & BARR, P. W. 1974 *Proc. 2nd Int. Workshop on Laser Velocimetry* (ed. W. H. Stevenson & H. D. Thompson). Purdue Univ. School Mech. Engng.

SIMPSON, R. L. & BARR, P. W. 1975 *Rev. Sci. Inst.*, **46**, 835–837.

SIMPSON, R. L., STRICKLAND, J. H. & BARR, P. W. 1973 *Symp. Turbulence in Liquids, Univ. Missouri-Rolla* (ed. J. L. Zakin & G. Patterson), pp. 151–171.

SIMPSON, R. L., STRICKLAND, J. H. & BARR, P. W. 1974 *Thermal Fluid Sci. Center, Southern Methodist Univ., Rep.* WT-3.

SO, R. M. C. & MELLOR, G. L. 1973 *J. Fluid Mech.* **60**, 43–62.

SOVRAN, G. 1969 *Comp. Turbulent Boundary Layers.* 1968 *AFOSR–IFP Stanford Conf.*, vol. 1 (ed. Kline *et al.*), pp. 447–455.

SPANGENBERG, W. G., ROWLAND, W. R. & MEASE, N. E. 1967 *Fluid Mechanics of Internal Flow* (ed. G. Sovran), pp. 110–150. Elsevier.

STRICKLAND, J. H. & SIMPSON, R. L. 1973 *Thermal Fluid Sci. Center, Southern Methodist Univ., Rep.* WT-2.

STRICKLAND, J. H. & SIMPSON, R. L. 1975 *Phys. Fluids*, **18**, 306–308.

TAYLOR, G. I. 1938 *Proc. Roy. Soc.* A **164**, 476–490.

TOWNSEND, A. A. 1962 *J. Fluid Mech.* **12**, 536–554.

WILLMARTH, W. W. 1975 *Adv. Appl. Mech.* **15**, 159–254.

WYGNANSKI, I. & FIEDLER, H. E. 1970 *J. Fluid Mech.* **41**, 327–361.

WYNGAARD, J. C. 1969 *J. Sci. Inst.* **2**, 983–987.